4. LARGE EDDY SIMULATIONS & RESULTS

In order to gain insight into the turbulent impinging jet flow, LES studies of a round impinging jet have been performed. The cases with different inflow conditions investigated are:

4.1 Fully developed turbulent jet (Re=23000)
4.2 Velocity field active excitation (Re=23000)
4.3 Velocity field passive excitation (Re=23000)
4.4 Temperature field excitation (Re=23000)
4.5 Swirling jet (Re=23000 & 21000)

4.1 LES of Natural Jet Impingement

This section describes the a-posteriori testing of an impinging jet case. A-posteriori Testing is defined as the benchmark testing of the LES code by simulating a problem with known experimental results and comparison of the predicted results with the measurements.

For purpose of investigation the case of orthogonally impinging round jet of Reynolds number (Re=U_bD/ν) 23000 is selected. The flow field was investigated experimentally by Cooper et al. [28] and heat transfer is investigated by Baughn et al. [13; 12]. It is also an ERCOFTAC's recommended test case (C.25), for testing turbulence models [43].

Computational Domain

A cylindrical domain is used for the investigation of an axisymmetric impinging jet. The jet issues from a pipe and strikes at the center of the circular target wall. A top confinement wall is used with no slip boundary condition. The wall jet forms as a result of impingement spreads over the target wall and flow leaves the domain from the outlet circumferentially. The computational setup resembles closely with the experimental setup utilized in number of experiments (see [13; 121]). Figure 4.1(a) shows a schematic diagram of the impinging jet phenomenon. The temperature at the pipe inlet is T_o. The temperature attained by the

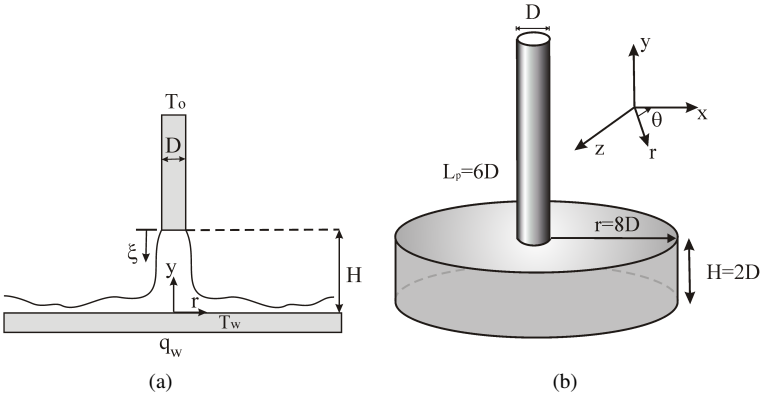

Figure 4.1: (a) Schematic diagram of the jet impingement phenomenon. (b) Computational domain.

target wall after the jet impingement is T_w. A constant heat flux (q_w) is applied at the target wall. The size of domain must be sufficiently large to capture all relevant large-scale structures. The computational domain consists of a cylindrical domain connected to a circular pipe as shown in figure 4.1(b). The length of the pipe is 6D, where D is it's diameter. The pipe outlet-to-wall distance (H) is 2D. The cylindrical domain is 16D in diameter.

The local heat transfer coefficient is defined as:

$$h = \frac{q_w}{\overline{T_w} - T_o}, \tag{4.1}$$

where T_o is jet inlet temperature, T_w is the target wall temperature and q_w is the heat flux at the wall, $\overline{(.)}$ indicates averaging. The Nusselt number is defined as:

$$Nu = \frac{\overline{h}D}{\lambda} \tag{4.2}$$

Numerical grid resolution

The mean grid spacing feasible for DNS simulation is $O(\eta)$, where η is the Kolmogorov scale. In LES, however, the grid estimation is not very clear as part of the flow field is modeled. In a pipe or channel flow, the low speed streaks are present in the near wall

region, which are estimated to be 1000 viscous wall units and in transverse direction 100 wall units. In the present simulation the streamwise direction in the pipe is 2πD which is equivalent to 7740 wall units. The grid constructed for the pipe has $\Delta L_p^+ = (\Delta L)_p u_\tau/\nu$=70.

At the impingement wall, the near wall grid fulfills the requirements of properly resolved direct numerical simulations. The mean grid spacing near wall Δ^+/η^+ is 6.6, where η is the length of the Kolmogorov scale. The most important domain region is the stagnation and wall jet region (r/D≤4), where the $\Delta r^+ = (\Delta r)u_\tau/\nu$ is ≈ 36 and $r\Delta\theta^+ = (r\Delta\theta)u_\tau/\nu$ ≈ 20. In the wall jet zone the maximum Δr^+ is 94.

To further check, the dissipation is estimated from the simulation and Kolmogorov scale is computed. It is found that inside the shear layer the mean grid spacing is of the order of 8η, which is very close to the earlier estimation.

Both the pipe and cylindrical domain are modeled via O-grids. The domain is divided into 42 blocks. In the investigations, the hexahedral structured grid have been used. Total 5 million control volumes are used for the simulation of this case.

Outlet Boundary Condition

As it is desired to simulate the non-linear temporal and spatial development of the turbulent impinging jet flow, the correct choice of the outlet boundary conditions is a crucial problem. The boundary condition used for the out-flow is a non-reflective or convective boundary condition. This allows a negligible influence on the evolution of the flow structures in the finite size interior of the computational domain. It is found that the use of Von Neumann type boundary conditions with a full three-dimensional domain Large Eddy Simulation, for the case under investigation, generates a non-physical feedback, which strongly affects the global stability of the flow field. The non-reflective, radiation, absorbing, or advective/ convective boundary condition is spatially and temporally local, and defined as [27]:

$$\frac{\partial U}{\partial t} + \Lambda \frac{\partial U}{\partial r} = 0 \tag{4.3}$$

The quantity Λ is taken to be a constant convection velocity of the large-scale structures, which is set to a constant as per global mass conservation requirements. This boundary condition has an upstream influence over about one dimensionless length, which is usually called a buffer zone.

Inlet Boundary Condition

A turbulent velocity signal has certain statistical properties, such as, mean values, fluctuations, cross correlations, higher order moments, length and time scales. In order to attain realistic turbulent inflow conditions the traditional approach is to perform a precursor

simulation, which satisfies the above mentioned characteristics. The data from this precursor simulation is transfered to the inlet plane of the following simulation. However, this demands extra computational resources and costs. Recently, there is a growing interest towards synthetically generating inflow conditions. In the present work, the approach proposed by Klein et al. [115] is used for the inflow turbulent conditions. The procedure is found to give good results and has been previously tested for plane jet flow by Klein et al. [115]. Wegner et al. [189] have used it for a jet in cross-flow, issuing from a circular pipe. It is also tested by the present author for a backward-facing step and found to be an efficient method.

In this procedure, the inflow turbulent velocity generated is based on the relation:

$$u_i = \overline{u_i} + g_{ij} U_j^{'}, \tag{4.4}$$

where $\overline{u_i}$ is the mean axial velocity at the inflow plane, $U_j^{'}$ are velocity fluctuations and g_{ij} is a tensor related to the Reynolds stress tensor (see [115]). The velocity fluctuations generated are based on digital filtering of random data. According to this procedure, the prescribed autocorrelation function R_{uu} for homogeneous turbulence in late stage is used to describe turbulence.

$$R_{uu}(\mathbf{r}) = exp\left(\frac{-\pi \mathbf{r}^2}{4(\ell(t))^2}\right) \tag{4.5}$$

where $\mathbf{r}$ is the position vector and ℓ(t)=$\sqrt{2\pi\nu(t-t_o)}$, is the integral length scale at the inflow plane. The fluctuation level is specified by DNS data. The fully developed turbulent pipe flow mean velocity profile together with the velocity fluctuations varying in time are prescribed at the inflow. The mean velocity profile is taken from Kays et al. [111]:

$$u^+ = 2.5ln\left[\frac{1.5y^+(1+r/r_w)}{1+2(r/r_w)^2}\right] + 5.5, \tag{4.6}$$

where y^+ is the pipe wall normal direction and r is the radius of the pipe.

To further check the accuracy of the procedure, the mean velocity at the pipe outlet is inspected and compared with the turbulent pipe flow simulation. The Reynolds number of pipe flow simulation corresponds to Re_D=23000. Since it is desired to investigate the efficiency of inflow turbulence generator and its utility as a general purpose tool, the pipe flow simulation is only utilized for comparison purpose and not used as a precursor simulation.

The temperature at inlet is set to 293 K.

Boundary conditions at walls

The pipe and top confinement wall were made adiabatic. At the bottom impingement wall, the constant wall heat flux of 1000 W/m^2 is applied. The no slip boundary condition is used

for all walls.

Solution Control

The flow inside the domain is monitored and it attains statistical stationary state after eight cycles, where one cycle corresponds to the natural frequency of the jet. Once the flow becomes statistical stationary, it is averaged in time and space. The simulation is controlled in such a way that the CFL number remains less than one. The dimensionless time step used is $\Delta t D/U_b$ equal to 7E-08. For the computation 20 processors were used. The computations were performed on the CRAY Opteron Cluster, Höchstleistungsrechenzentrum (HLRS), Stuttgart, Germany.

Results

This sections contains the details of the results and discussion. First the energy spectrum is investigated and the frequencies present inside jet are investigated then the velocity distributions in the wall jet along with turbulent intensities are explored. The budget of turbulent kinetic energy and anisotropy invariant mapping is used to explain the nature of turbulence in impinging jet. Although the computations were done in Cartesian coordinate system, the results are presented in special Cylindrical coordinates (r, θ, y) system, where r is the radius of the computational domain. In the following section U represents the mean velocity and defined as:

$$U = \sqrt{\overline{u_r}^2 + \overline{u_\theta}^2 + \overline{u_y}^2},$$

where, $\overline{u_r}$, $\overline{u_\theta}$ and $\overline{u_y}$ represent the velocity in radial, azimuthal and vertical directions respectively. The subscripts $(.)_b$ and $(.)_{CL}$ represent the bulk and centerline velocity at the pipe's exit.

Instabilities in an axisymmetric jet

The large scale structures originating from the shear layer instabilities of a Kelvin Helmhotz (KH) type, significantly affect the later development of the jet. The KH instabilities which exist between the fast moving jet flow and surrounding slow moving fluid, also enhance the entrainment of the surrounding fluid. The instabilities give rise to the formation of the Ring vortex, shown in figure 4.2.

The contours of the vorticity magnitude shows the development of the initial shear layer. The resolution of the initial shear layer is important for the development of instabilities in the jet. The reader is referred to the schematic diagram of instabilities growth in an axisymmetric jet by Yule [198] presented in figure 1.9(a). The Large Eddy Simulation corroborates

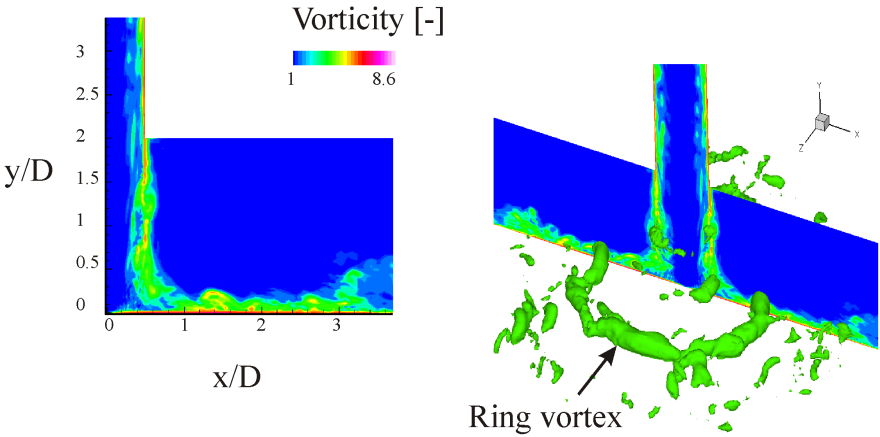

Figure 4.2: Ring vortex visualized through iso-pressure surfaces ($P/\rho U_b^2$ = -0.016) and the contours of the instantaneous total vorticity ($\omega D/U_b$) in the jet's shear layer.

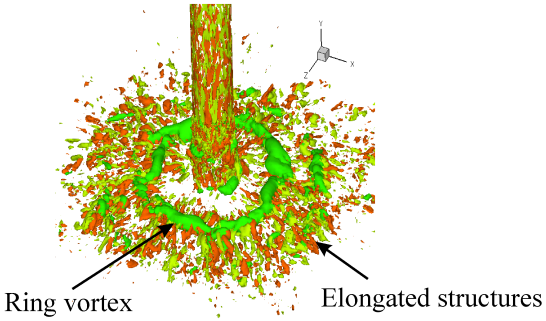

Figure 4.3: Elongated structures revealed through iso-vorticity surfaces ($\omega_y = \pm 3.8 U_b/D$). The orange structures represent the positive vorticity and yellow shows the negative vorticity regions. The ring vortex is shown in green color.

the earlier findings of the researchers. As can be noted, the vorticity containing fluid emanates from the pipe wall and forms the shear layer. Figure 4.3 shows the coherent structures extracted through iso-vorticity surfaces. In a free jet the vortex rings are connected by these structures [125]. The intermittently generated toroidal shaped (ring) vortices, lose their structure on striking the surface and the iso-vorticity structures are stretched. Single point statistics explain the behavior of structures in a turbulent impinging jet, which is discussed in the next section.

Velocity Spectra and Preferred mode of Axisymmetric jet

If a jet emerges from a converging nozzle and the boundary layer on the inner surface of nozzle is laminar, the initial region of a jet shear layer can be considered as parallel or two dimensional. In this case, the ratio of the jet diameter to the initial momentum thickness is large (ζ/D $<$ 1 - 1.5), where ζ is the distance from the nozzle or pipe outlet. The shear layer near the nozzle is initially dominated by a Kelvin Helmholtz instability mechanism. This would cause the formation of the first vortex at the nozzle lip. The formation of a vortex is attributed to most amplified frequency of small disturbances which grow exponentially [95]. This mode represented by the Strouhal number (scaled with momentum thickness) is called shear layer mode [95], in terms of a dimensionless frequency it can occur in the range of Strouhal numbers $St_{\delta^{**}} = f_o \delta^{**}/U_o = 0.01$ - 0.018 [73], where δ^{**}, is the momentum thickness of the boundary layer.

However, if the jet emerges in a fully developed flow state from a long pipe, the momentum thickness is of order of the jet radius and the jet does not exhibit the shear-layer mode, instead it will attain the jet column mode. In jet column mode the frequency is scaled with diameter of the jet. The most amplified frequency represented by the Strouhal number (scaled with diameter) is called the preferred mode of the jet, corresponding to the Strouhal number range St_D= 0.25 - 0.85 [181; 128].

Liu & Sullivan have found that the natural frequency of an impinging jet is the same for a free jet if ζ/D $>$ 1 [128]. Olsson & Fuchs have found that the mean velocity and turbulence intensity in an impinging jet starts to differ from those in a free jet at a distance of about 1.3D from the wall [149]. Tsubokura et al. also found that the natural frequency in the impinging jet corresponds to St_D equals to 0.37 [183].

In order to investigate the most amplified frequencies in the jet, the data is monitored simultaneously inside the jet core, shear layer, impingement zone and wall jet region. The most amplified frequency is found inside the shear layer at the distance (ζ) equals one pipe diameter, downstream of the pipe outlet. This corresponds to a Strouhal number of 0.328 (preferred mode of the jet). The most amplified frequency of jet instability predicted by LES lies in the known range of Strouhal numbers which can be taken as an indication of right resolution requirements.

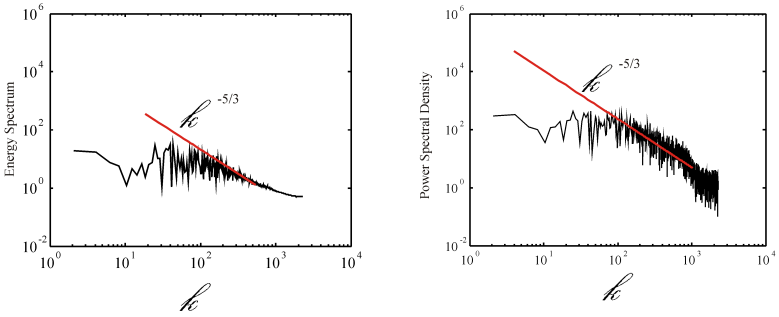

(a) (b)

Figure 4.4: (a)Turbulence energy spectrum and (b) Power spectral density in jet shear layer, the line indicates the slope of the inertial subrange.

An important issue in LES is the determination of whether the turbulent scales are resolved or not. It is interesting to note that although the turbulence at the inflow is specified artificially, it matches well the known characteristics of the turbulence spectrum. Figure 4.4 (a) shows the energy spectrum and figure 4.4 (b) the power spectral density at the same point. The slope of the spectrum $(-5/3)$ indicated by the straight line in figure 4.4 agrees well with the known characteristics of turbulence spectrum. The energy spectrum shows that the energy does not build up at higher wave numbers.

Figure 4.5 shows the turbulence spectrum close to wall in the wall jet zone near the stagnation point. The fluctuations in the velocity field go to zero as the wall is approached. Nishino et al. have found that the flow near the stagnation point is isotropic in nature. The slope of the spectrum corroborates these findings.

The single point data gives the information about the frequencies present at that particular location. However, the common frequencies present at two different stations is also an interesting inquiry. The information about the common frequencies is obtained by plotting the coherency spectrum of the velocity fluctuations at two spatial positions (spaced r/D=1/2) in the jet shear layer (located at ξ/D=0.05,1.5 and 1.90). The coherency spectrum is defined as [177]:

$$Coh(f) = \left| \int_{-\infty}^{\infty} C_{u_y u_y}(\Delta t) e^{-2\pi i f \Delta t} d(\Delta t) \right| \tag{4.7}$$

where $C_{u_y u_y}(\Delta\,\mathrm{t})$ is the two time correlation $\overline{u'_{y,a}(t) u'_{y,b}(t+\Delta t)}$ and $u'_{y,a}$, $u'_{y,b}$ are the velocity

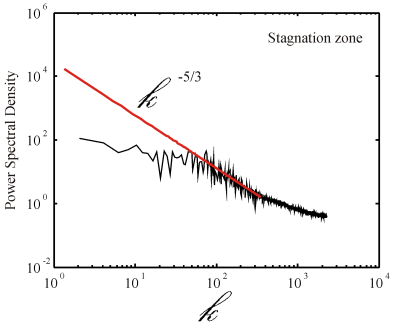

Figure 4.5: The turbulence spectrum close to wall in wall jet zone near stagnation point. The line indicates the slope of the inertial subrange.

fluctuations at two different positions. The coherency spectrum reduces the influence of the broadband background energy and increases the discrete frequencies present [177]. Therefore common frequencies at these particular locations can be investigated by the analysis of coherency spectrum.

Figure 4.6(a) shows the coherency spectrum of velocity fluctuations at two different stations at the same level in the shear layer of the jet. The dotted line shows the frequencies present at the pipe outlet. The solid line shows the frequencies present at a distance of one jet diameter. The Coh(f) at ξ/D= 1.5 is larger than at ξ/D= 0.05. This shows that the frequencies are amplified as the free jet develops. Figure 4.6(b) shows the frequencies in deflected jet near the target wall. There are several harmonic peaks present in the deflected jet spectrum, which indicate that several structures are present near the wall, which contain less energy than the structure in the free jet.

Mean flow properties and turbulent flow intensities

The mean velocities & turbulent fluctuations from the Large Eddy Simulation have been compared with the following experimental data:

1. Cooper et al. (Re=23000 & H/D=2) (Hot wire anemometry)[28]
2. Hargrave et al. (Re=23340 & H/D=2) (Particle Image Velocimetry) [80]
3. Geers et al. (Re=20000 & H/D=2)(Particle Image Velocimetry)[61]

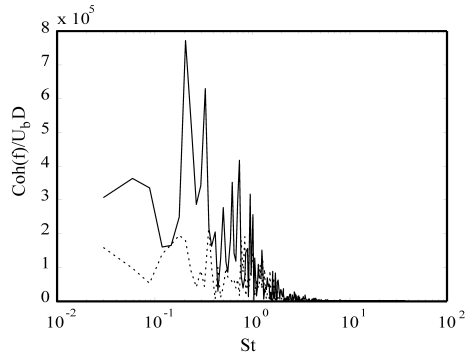

(a)

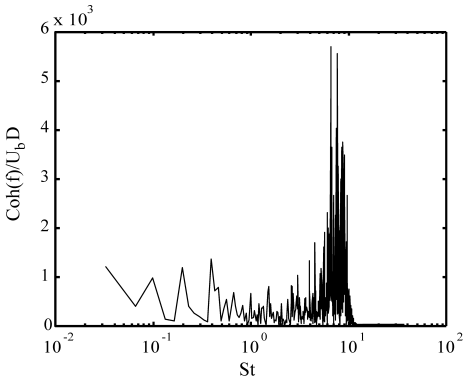

(b)

Figure 4.6: Coherency spectrum of the velocity fluctuations in the jet shear layer. (a) The dotted line shows the frequencies present at the pipe outlet (ξ/D =0.05). The solid line shows the frequencies present at ξ/D=1.5. (b) The figure shows the frequencies in the deflected jet, above the impingement wall (ξ/D=1.90). The coherency spectra is normalized by the pipe diameter and the bulk velocity of the pipe flow.

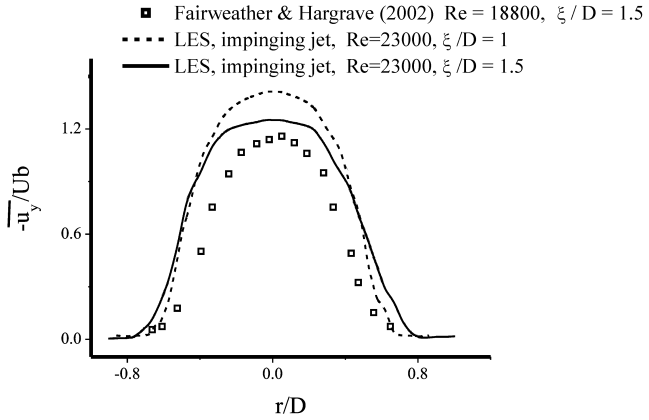

Figure 4.7: Jet mean axial velocity compared with experimental data of Fairweather & Hargrave (Re=18800).

4. Fairweather et al. (Re=18800 & H/D=2) (Particle Image Velocimetry)[44]

The velocity distribution inside the free jet at the distance of ξ/D=0.5 is shown in figure 4.7. Although, the Reynolds numbers of the experiment is different from the one in simulation, the agreement between the trend of the velocity distribution is promising. The jet velocity reduces as the target wall is approached.

The simulated velocity field is shown in figure 4.8. One can see that the velocity of the jet reduces as the jet approaches the wall. At the stagnation zone the velocity goes to zero. The flow accelerate radially outward and the near wall velocities are higher than the main jet velocity. The unsteadiness in an impinging jet causes the entrainment of the surrounding fluid.

Geers et al. have given the mean velocity distributions in a single impinging jet at r/D=0, (i.e. stagnation line) and at r/D=0.5 [61]. Figure 4.9, 4.10 and 4.11 show a comparison between PIV and LDA measurements with the current Large Eddy Simulation. Good match has been found in the results. The mean radial velocity $\overline{u_r}$ is almost zero, which shows the axial symmetry.

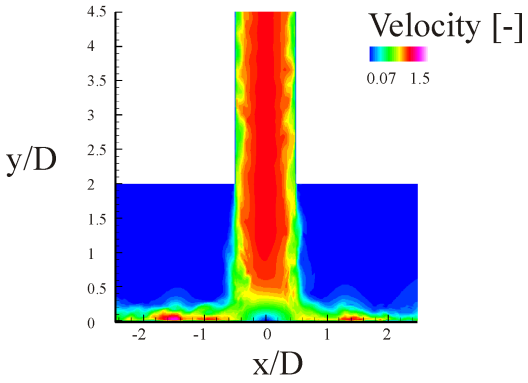

Figure 4.8: Instantaneous velocity field U/U_b in an impinging jet.

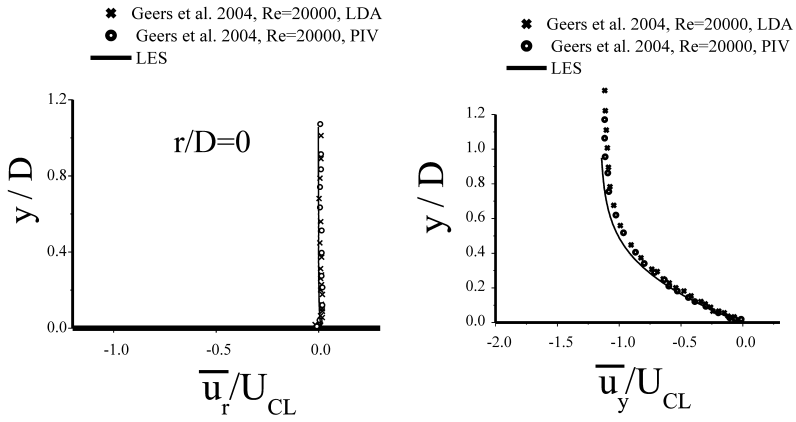

Figure 4.9: Components of mean velocity $\overline{u_r}/U_{CL}$ and $\overline{u_y}/U_{CL}$ at r/D =0, solid line (LES), ○ PIV, × LDA measurements of Geers et al.[61], U_{CL} is the velocity at the centerline at jet's exit.

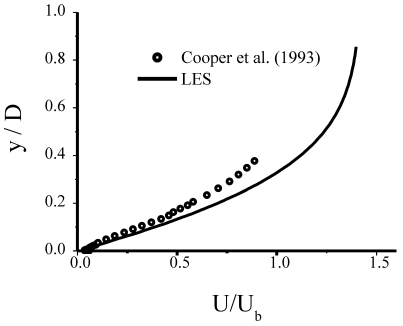

Figure 4.10: Mean velocity U/U_b at r/D =0, solid line (LES), ○ hot wire measurements of Cooper et al. [28], U_b is the bulk velocity at the jet exit.

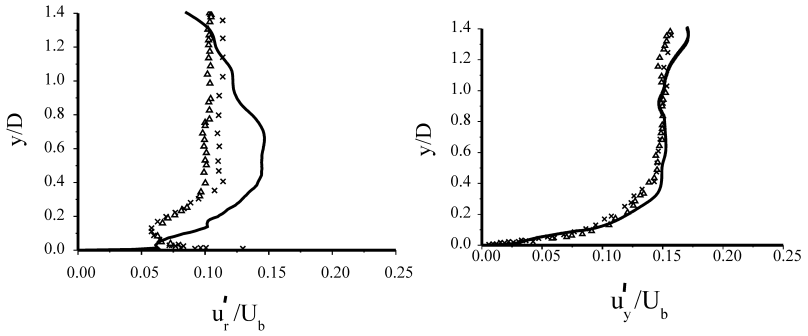

Figure 4.11: Root mean velocity fluctuations $u_r^{'}/U_{CL}$ and $u_y^{'}/U_{CL}$ at r/D =0.5, solid line (LES), △ PIV, × LDA measurements of Geers et al. [61], U_b is the velocity at jet's exit.

The velocity and turbulent fluctuations in the wall jet are compared with the data by Cooper et al. [28]. The Large Eddy Simulation agrees well with experiments. Figure 4.12 and 4.13 show the comparison between simulation and experiments in the wall jet zone. The distribution of turbulent stress in wall jet region is shown in figure 4.13(c). According to Cooper et al. [28], root mean square fluctuating velocities have the experimental measurement uncertainties of $\pm$ 4% ($u_r^{'}$), $\pm$ 6 % ($u_y^{'}$) and shear stresses ($u_r^{'}u_y^{'}$) have uncertainiites of $\pm$ 9%. Close to wall the agreement between the shear stresses and wall normal velocity fluctuations is very good. The radial velocity fluctuations agree with the experimental data as the jet develops.

It is interesting to note that the turbulent stress does not vanish at a point where the velocity gradient is zero. The same phenomenon is observed by Poreh et al. [162] through experimental measurements. The eddy viscosity hypothesis based turbulence models assume that the turbulent shear stress is proportional to the local gradient of the mean velocities. As found through current simulation this assumption is invalid for the wall jet zone. The mean velocity is found to be maximum at y/D equals 0.0314, where the shear stress $\overline{u_r^{'}u_y^{'}}$ is not zero.

Note that although the trend of the turbulent flow intensities distribution are in agreement with the experimental data the magnitude of the predicted turbulent intensities are higher than hot-wire measurements. The reason of this is not clear. It is known that in many cases the LES with subgrid models (including Germano's dynamic Smagorinsky model) over-predicts the turbulent velocity fluctuations, especially in the wall bounded flows [22]. Further, the hot wire measurements are well known for generation of erroneous data in regions of high turbulence. They also under-predict the turbulence level, probably due to their intrusive flow measurements.

Figure 4.12 and 4.13 (a) shows the differences in the predicted turbulent radial velocity fluctuations from the experiments. On the other hand, the agreement between the vertical velocity fluctuations and shear stresses with the experiments is quite good, as can be seen in figure 4.13 (b) and (c).

Law of the wall for wall jet zone

The wall jet developing after impinging jet does not exhibit the conventional law of the wall behavior. The following semi-logarithmic relation can be used to model the inner layer of the wall jet:

$$u^+ = \frac{u}{u_\tau} = \frac{1}{\kappa} ln(\frac{y u_\tau}{\nu}) + B \tag{4.8}$$

where u_τ is the friction velocity and κ is the von Karman constant.

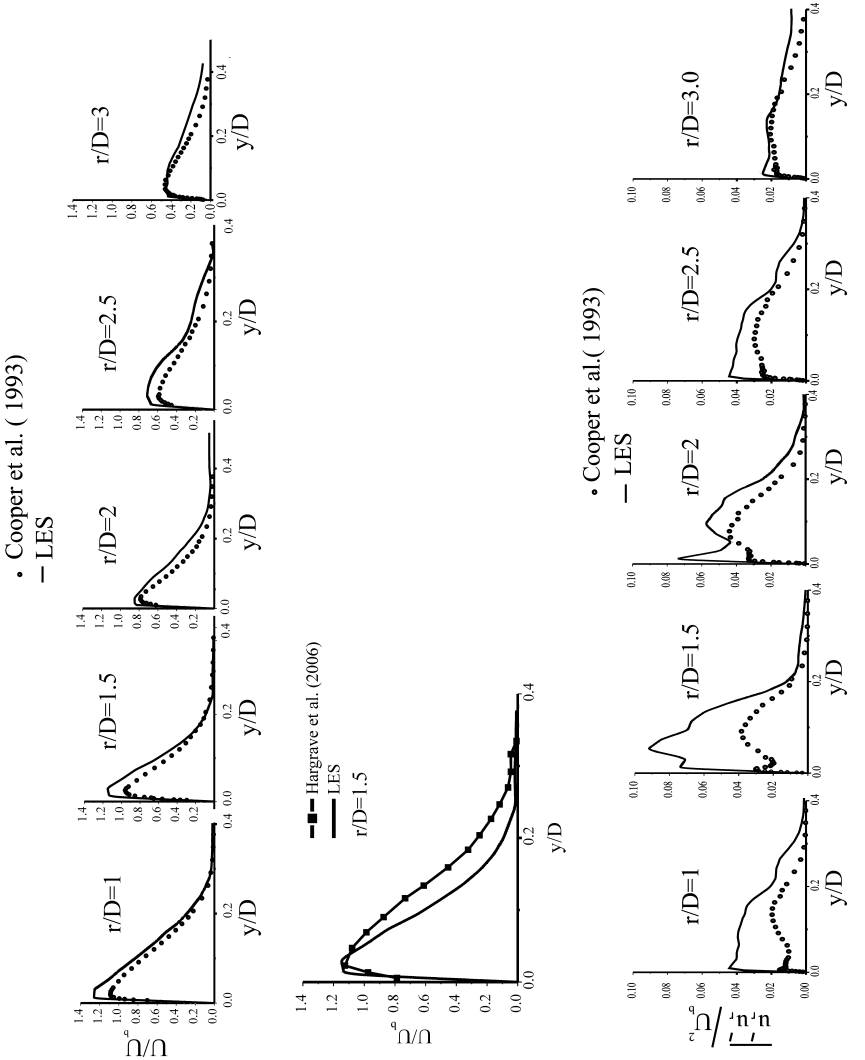

Figure 4.12: Velocity U/U_b and streamwise fluctuations $\overline{u_r' u_r'}/U_b^2$ in the wall jet, solid line (LES), ∘ Hot-wire measurements of Cooper et al. [28], Filled-box PIV measurements of Hargrave et al. [80], U_b is the bulk velocity at jet's exit.

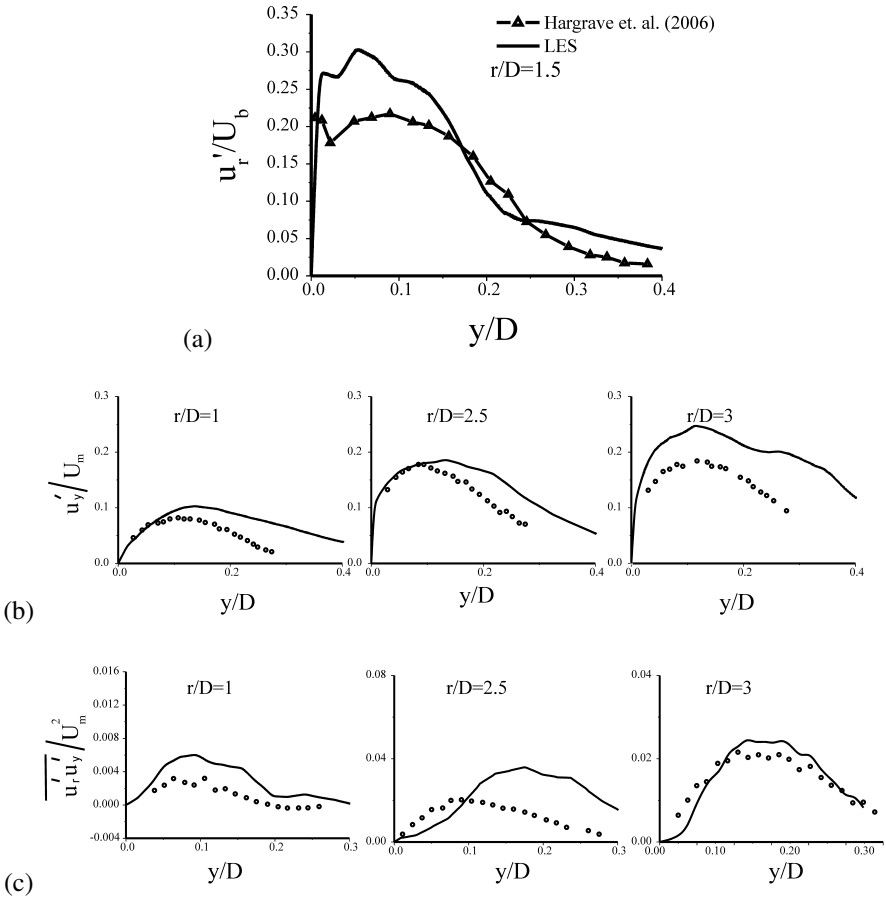

Figure 4.13: Root mean velocity fluctuations (a) $u_r^{'}/U_b$, (b) $u_y^{'}/U_m$ and shear stresses (c) $\overline{u_r^{'}u_y^{'}}/U_m^2$ in wall jet , solid line (LES), ∘ Hot-wire measurements of Cooper et al. [28], △ PIV measurements of Hargrave et al. [80], U_b is the bulk velocity at jet's exit & U_m is the local maximum velocity in wall jet region.

Wygnanski et al. [194] have found that a logarithmic profile might be fitted to the data but the constant (B) present in the law of the law must be adjusted. Özdemir and Whitelaw [150] have found that in case of an impinging jet, if the outer edge of the equilibrium layer is attached to the point of maximum velocity (U_m), which occurs close to wall, then this maximum velocity can be used as an appropriate scaling parameter. They stated that in above relation B can not be treated as a constant rather it is a function. They proposed the following formulation:

$$B = f(\frac{U_m}{u_\tau}) \tag{4.9}$$

Using the approach proposed by Özdemir et al. [150] and Guerra et al. [63] the following relationship is obtained:

$$B = 1.122(\frac{U_m}{u_\tau}) - 10.53 \tag{4.10}$$

The first term in the above equation is called profile shift parameter. If this shift parameter is subtracted from the law of the wall, the resulting curve shows the presence of an equilibrium layer that extend up to the point of maximum velocity. Figure 4.14 (a) and (b) shows the radial velocity profiles with and with out subtracting the shift parameter in semi-logarithmic axes.

The simulation thus confirms the previous experimental findings of [150] and [63] that the inner layer of the wall jet, which is formed after the jet impingement on the wall, can be cast in to scaling log-laws. As can be seen, the flow in an impinging jet and the subsequent wall jet is highly complex. It is found that the mean flow characteristics are influenced by the wall shear stress. It is important to analyse the nature of the turbulence in detail, which is the subject of the next section.

Anisotropy invariant mapping

One of the subtle problems in Large Eddy Simulations is the use of correct formulation for the near-wall behavior of turbulent flow. Numerous wall-models are proposed for the Large Eddy Simulations (see section 2.3.2). However, most of these near-wall models are based on the ideas taken from channel flows. The anisotropy invariant mapping is a nice tool to investigate the near wall behavior of the turbulent flow. The Reynolds stress anisotropy tensor is defined as:

$$b_{ij} = \frac{\overline{u_i' u_j'}}{2k} - \frac{\delta_{ij}}{3} \tag{4.11}$$

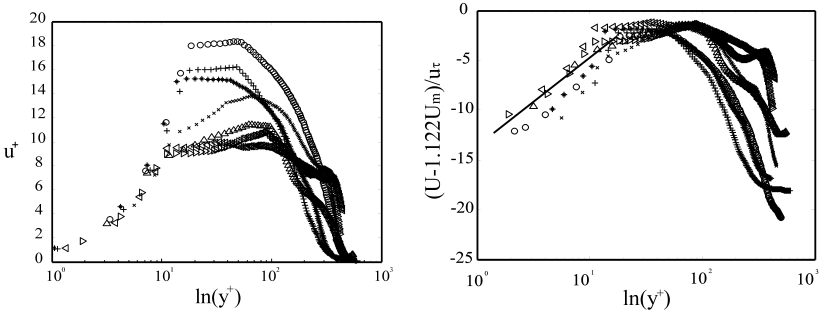

(a) (b)

Figure 4.14: (a) Semilogarithmic plot of the radial velocity profiles with out subtracting the shift parameter, (b) Velocity profile with subtraction of profile shift parameter, the line shows the characteristic of the equilibrium layer that it extend till the location of maximum velocity.◯ r/D=1, + r/D=1.5, ∗ r/D=2, × r/D=2.5, ◁ r/D=3, ▷ r/D=3.5, △ r/D=4.

where the turbulence kinetic energy is defined as:

$$k = \frac{1}{2}\overline{u_i' u_i'} \tag{4.12}$$

It is clear from the equation 4.11 that none of the eigenvalues of the anisotropy tensor b_{ij} can be larger than 2/3 and none can be smaller than 1/3. Therefore, all possible turbulence states can be described by the turbulence triangle in invariant coordinates.

Any function of invariants of a tensor is independent from rotations of the coordinate system. The first invariant is the sum of the diagonal components. The second and third invariants denoted by II and III are defined as:

$$-II = b_{ij} b_{ij}/2 \tag{4.13}$$

$$III = b_{ij} b_{jk} b_{ki}/3 \tag{4.14}$$

The fact that the invariants do not change with rotation of the coordinate system, make them a valuable tool for the turbulent flow analysis.

Figure 4.15 shows the AIM plot of a pipe flow obtained from the experimental data by Krogstad and Torbergsen [114]. The flow near the wall is following the two-component

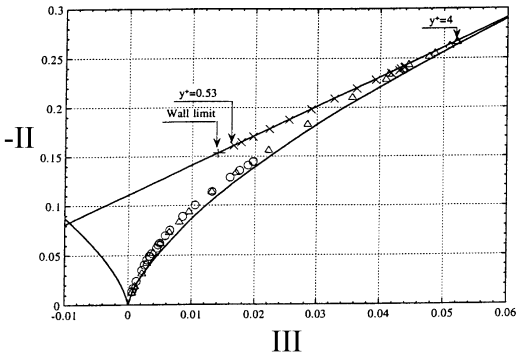

Figure 4.15: Anisotropy invariant map of the Reynolds stresses near pipe wall obtained from experimental data, ○ Krogstad and Torbergsen [114] Re_D= 22000, △ DNS Eggels et al. [42], Re_D= 5300, × DNS channel data of Kim et al. [110], Re_D= 3300. lines indicate the region for realizable turbulence states (adapted from [114]).

state. Above the surface after y^+>4, the flow is following the axisymmetric expansion state. Eggels et al. [42] found differences between pipe and channel flows, based on direct numerical simulations.

Nishino et al. [147] have utilized the anisotropy invariant map (AIM) for the investigation of the nature of turbulence in the stagnation zone of an impinging jet. They found that the flow near a wall is in an isotropic state. The turbulence is following the axisymmetric contraction state below y/D =0.1 (or ξ/D = 1.9). However, after y/D= 0.1 (or ξ/D = 1.9) the turbulence is in an axisymmetric expansion state. Figure 4.16 shows the AIM plot from experimental data by Nishino et al. [147]. The AIM shows that near wall flow in pipe/channel flow is very far from near wall flow in case of an impinging jet. Therefore it is expected that the existing wall models might not work well with the impinging jet Large Eddy Simulation.

In the wall jet, $\overline{u_r' u_r'}$ is larger than $\overline{u_y' u_y'}$ and $\overline{u_\theta' u_\theta'}$. This causes the anisotropy tensor b_{11} larger than b_{22} and b_{33}. It has been found that at r/D=2 the flow near wall is also nearly isotropic, as the IIIrd invariant is very small. The turbulence is following an axisymmetric contraction state below y/D =0.02. However, after y/D= 0.02 the flow is in an axisymmetric expansion state. The AIM at r/D=2 is plotted in figure 4.17. Later at $r/D \approx$ 4 the near

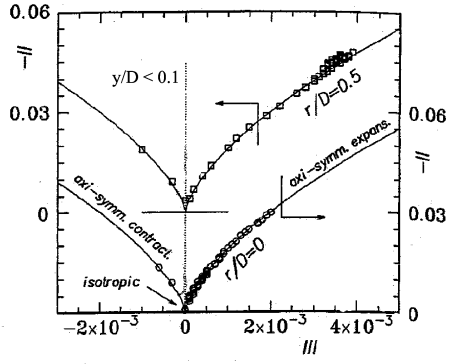

Figure 4.16: Anisotropy invariant map of the Reynolds stresses near impingement wall at Re= 10400 and 13000 and H/D= 5.86, ○ at r/D= 0, □ at r/D= 0.5. (adapted from Nishino et al. [147])

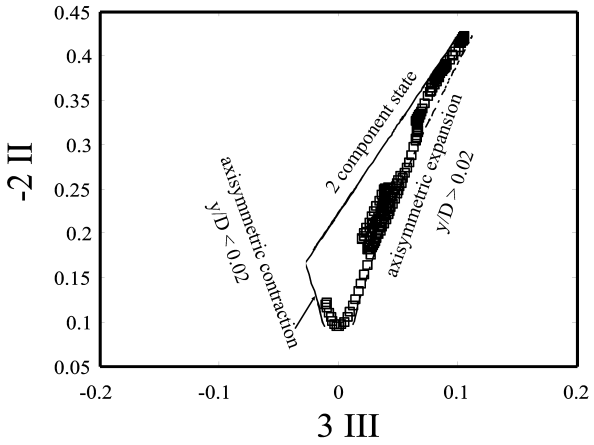

Figure 4.17: Anisotropy invariant map of the Reynolds stresses at r/D=2, ○ shows the simulation data, lines indicate the region for realizable turbulence states.

wall flow becomes non-isotropic. The isotropic flow region moves away from the wall. This is consistent with the known behavior of the wall jet, as the flow near the wall is highly anisotropic. It is important to note that RANS based turbulence models with the assumption of isotropy may not perform good in the near impingement wall jet zone. Only the Reynolds stress model (RSM) account the anisotropic flow behavior. However, they too do not give acceptable results for the impinging jet case. This indicate that the better modeling approaches for anisotropy in flow field are required for acceptable predictions of the flow field through the RANS based turbulence models. The above analysis reveal that the flow near the wall is highly complex. In order to understand the near wall flow field further the budgets of turbulent kinetic energy are investigated in the next section.

Budgets of turbulent kinetic energy

Reynolds stress equations can be written as:

$$\begin{aligned}
&\underbrace{\left(\frac{\partial \overline{u_i' u_j'}}{\partial t} + U_k \frac{\partial \overline{u_i' u_j'}}{\partial x_k}\right)}_{C_{ij}} = \underbrace{-\left(\overline{u_i' u_k'} \frac{\partial U_j}{\partial x_k} + \overline{u_j' u_k'} \frac{\partial U_i}{\partial x_k}\right)}_{P_{ij}} \\
&\underbrace{-\frac{\partial}{\partial x_k}\left[\overline{u_i' u_j' u_k'} + \frac{1}{\rho}(\overline{p' u_i'}\delta_{jk} + \overline{p' u_j'}\delta_{ik}) - \nu \frac{\partial \overline{u_i' u_j'}}{\partial x_k}\right]}_{dij} \\
&\underbrace{+\overline{\frac{p'}{\rho}\left(\frac{\partial u_i'}{\partial x_j} + \frac{\partial u_j'}{\partial x_i}\right)}}_{\Phi_{ij}} \\
&\underbrace{-2\nu\left(\overline{\frac{\partial u_i'}{\partial x_k}\frac{\partial u_j'}{\partial x_k}}\right)}_{\varepsilon_{ij}}
\end{aligned} \tag{4.15}$$

where C_{ij} denotes convection, P_{ij} denotes generation due to shear and force field, Φ_{ij} means redistribution effects of pressure fluctuations, d_{ij} is the diffusive transport, ε_{ij} is the viscous dissipation.

The trace of the above equation gives the turbulent kinetic energy and can be written

as:

$$\underbrace{\left(\frac{\partial k}{\partial t}+U_j\frac{\partial k}{\partial x_j}\right)}_{C_k}=\underbrace{-\left(\overline{u_i'u_j'}\frac{\partial U_i}{\partial x_j}\right)}_{P_k}$$
$$\underbrace{-\frac{\partial}{\partial x_j}\left[\frac{1}{2}\overline{u_i'u_i'u_j'}+\frac{1}{\rho}\overline{p'u_i'}\delta_{ij}-\nu\frac{\partial k}{\partial x_j}\right]}_{d_k}\underbrace{-\nu\left(\overline{\frac{\partial u_i'}{\partial x_j}\frac{\partial u_i'}{\partial x_j}}\right)}_{\varepsilon_k} \tag{4.16}$$

where C_k denotes convection, P_k denotes generation due to shear and force field, d_k is the diffusive transport, ε_k is the viscous dissipation.

An important quantity in the above equation is the production of the turbulent kinetic energy (P_k), which can be obtained by trace of the above equation. The term P_{ij} represents the continual extraction of energy from mean flow by the action of Reynolds stresses. The presence of negative production indicates the transfer of energy from turbulent field to the mean field. The radial distribution of the production of turbulent kinetic energy is plotted in figure 4.18. The contribution of production of turbulent kinetic energy in radial direction is higher than the others. It is found that in the wall jet the turbulent kinetic energy production is maximum approximately at around r/D equals 1.77. The radial distribution of production rates quickly reveal that $P_{\overline{u_r'u_r'}}$ plays a dominating role.

Through both experiments and Direct Numerical or Large Eddy Simulations it is found that there is a negative production of turbulence kinetic energy in the stagnation zone [147; 61; 169; 30; 78]. Satake and Kunugi [169] have conducted a DNS simulation of an impinging jet at Re =10000 and H/D = 6. They found that the production of turbulent kinetic energy is negative in the near-wall region in the stagnation zone. Nishino et al. [147] have found through experiments of an impinging jet at Re = 10400, 13000 and H/D = 5.86 that the production of turbulent kinetic energy is negative in the near-wall region. At these H/D ratios, the secondary peak in the radial distribution of Nusselt number is not present. It is found through present LES (Re =23000, H/D = 2) that close to wall the production of the turbulent kinetic energy becomes negative not only at stagnation point but also at the secondary peak.

The budgets of turbulent kinetic energy are plotted in figure 4.20. At the wall the dissipation is balance by pressure diffusion and turbulent diffusion. It has been found that pressure diffusion is playing a significant role in turbulent impinging jets, controlling the dynamics of the flow at the wall. This corroborates the earlier findings of Kataoka et al. [108] that the large scales eddies of surface pressure turbulence play an important role. Close to the jet's outlet, inside the jet's shear layer, the dissipation is balanced by production of turbulent kinetic energy. However as the jet develops and moves towards the target wall, the pressure diffusion becomes important and at the wall the dissipation is balance by

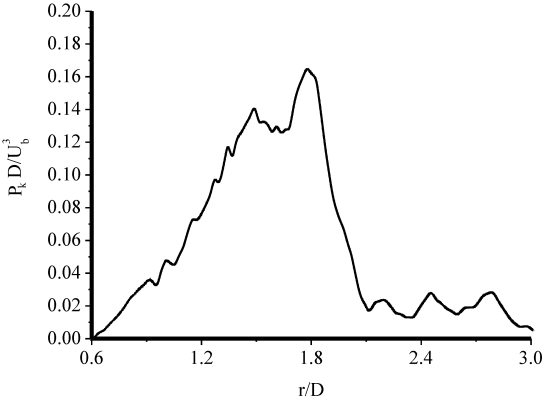

Figure 4.18: Production rate of turbulent kinetic energy (P_k) near impingement plate (y/D=0.08), all the values are normalized with U_b^3/D.

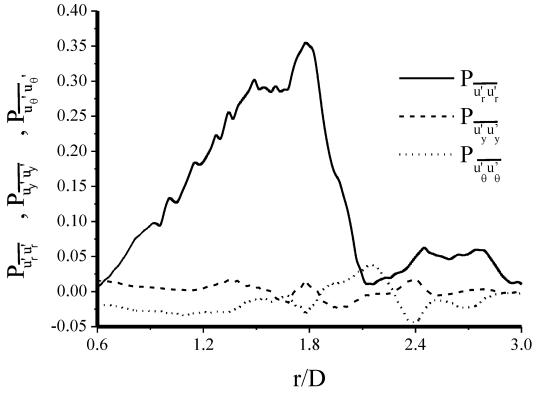

Figure 4.19: Contribution of the normal stress to the Production rate of turbulent kinetic energy near impingement plate (y/D=0.08), all the values are normalized with U_b^3/D. The solid line shows the contribution of ($P_{\overline{u_r'u_r'}}$), the dashed line shows the contribution of ($P_{\overline{u_y'u_y'}}$) and dotted line shows the contribution of ($P_{\overline{u_\theta'u_\theta'}}$).

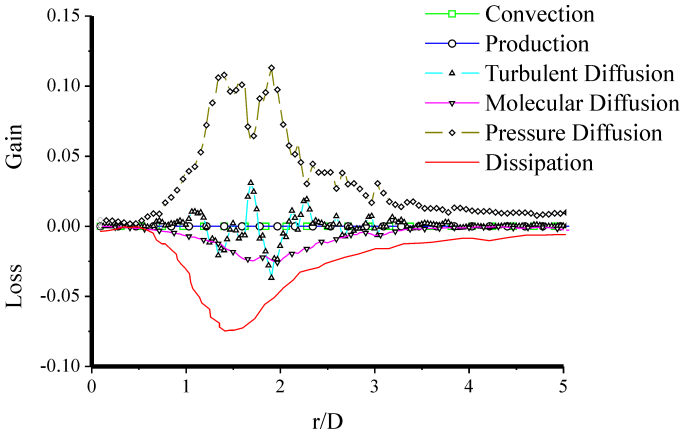

Figure 4.20: The budgets of turbulent kinetic energy at the wall, all the values are normalized with U_b^3/D. The solid line shows the contribution of dissipation, □ convection, ◯ production, ◇ Pressure diffusion, △ Turbulent diffusion, ▽ Molecular diffusion.

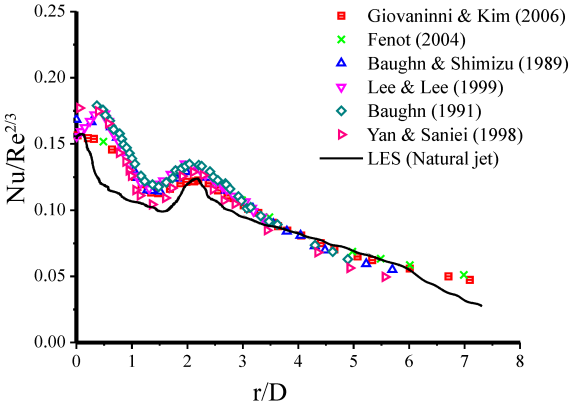

Figure 4.21: Radial distribution of the Nusselt number in an impinging jet, Re=23000 and H/D=2, Nusselt number is normalized with $Re^{2/3}$ □ ([65], $Re = 23000$), ◯([47], $Re = 23000$), △ ([12], $Re = 23750$), ▽ ([121], $Re = 20000$), ◁ ([13], $Re = 23300$), ▷([195], $Re = 23000$), solid line LES, $Re = 23000$.

pressure diffusion and turbulent diffusion.

Radial distribution of Nusselt number

Radial distribution of the Nusselt number predicted by the simulation is plotted in figure 4.21. The distribution is obtained after averaging in time and in space. For time averaging, the data after each 10 time steps has been used. For spatial averaging simulation data after 20 time steps is taken and ensemble-averaged at radial locations. As in some experiments, the jet's Reynolds number is different from 23000, it is necessary to remove the effect of Reynolds number. Therefore, the Nusselt number distribution is normalised by $Re^{2/3}$, which is recommended by Martin [133].

As one can see, the first peak Nu_1 is slightly off-set towards the stagnation point. However, the secondary peak is captured well. The differences in experimental data and simulation are high from r/D= 0.5 to about 1. However, the scatter in experimental data is also very high over there, indicating the complex dynamics of the flow over there.

For H/D equals 2, Lee and Lee [121] have found that the following relationship be-

tween the local peaks hold:

$$Nu_2/Nu_1 = 0.613 Re_D^{0.023} \tag{4.17}$$

From simulation it is found that the ratio between the two peaks Nu_2/Nu_1 is found to be 0.76, this agrees well with the correlation proposed by Lee and Lee [121] according to which the ratio is 0.77, for Re=23000 and H/D=2.

As can be seen, LES under-predicts the heat transfer in the stagnation zone (r/D < 1). It could be reasoned that this drop in the radial distribution of the Nusselt number is due to the prescription of mean velocity via semi-empirical relation defined by equation 4.6. The velocity prescribed by such a procedure is only an approximation to the true velocity. However, as the jet strikes the surface and the wall jet develops the influence of jet's mean velocity diminishes. Therefore, for r/D > 1 locations, both flow and heat transfer predictions are in good agreement with the experimental data.

Coherent structures and passive scalar-flux field

Yule [198] has defined the coherent structures as large eddies which are repetitive in structure, remain coherent for distances downstream very much greater than their length scales and contribute greatly to the properties of the turbulent flows, in particular, turbulence energy, shear stresses, entrainment and mixing. Several parameters have been proposed for coherent structures visualisation like iso-enstrophy and eigenvalue of the pressure hessian fields. The enstrophy ($1/2 \int_S \omega^2 dS$, where S is surface and ω is vorticity helps in detecting vortex layers that are predominant near the wall but cannot help in distinguishing them from cylindrical vortex tubes because enstrophy is defined by the square of vorticity. Therefore the enstrophy is effective in an isotropic turbulent flow but not effective for detection in a wall turbulent shear flow. In order to investigate the role of the coherent structures, two different methods, namely, iso-pressure surfaces and Q-criterion have been utilized. Through simulation it has been found that the ring vortices were found to be generated more or less periodically and striking the surface. This causes a constant oscillation of flow near the stagnation zone. Popiel and Trass [159] have found from visualisation studies that the fluid in the vicinity of the stagnation point experiences a pulsation due to swelling and contraction of the jet core. Hadžiabdić [78] has suggested that the constant precessing in this zone might be the reason for the high stagnation point heat transfer. The simulation corroborates these findings. It has been found that at r/D=1 the ring vortices are striking the surface which are causing a low pressure over there. At the same location, locally the velocity attains highest values in the impingement system. The periodic acceleration of the flow in this zone causes a boundary layer excitation, which increases the boundary layer thickness and hence reduces the temperature over there. As the ring vortex breaks up due to radial

stretching, the velocity increases and causes the local cooling effect on the wall. This causes an increase in heat transfer rate. The heat transfer rate reaches its maximum at r/D equals to two, which is normally attributed to the increase in turbulent kinetic energy. In order to understand the flow dynamics in this zone, the Q-criterion is used. The Q definition method is defined as [90]:

$$Q = \frac{1}{2}(\Xi_{ij}^2 - S_{ij}^2) \tag{4.18}$$

where S_{ij} and Ξ_{ij} are the symmetric and antisymmetric parts of the velocity gradient tensor, defined as,

$$S_{ij} = \frac{1}{2}\left(\frac{\partial u_i}{\partial x_j} + \frac{\partial u_j}{\partial x_i}\right), \tag{4.19}$$

and

$$\Xi_{ij} = \frac{1}{2}\left(\frac{\partial u_i}{\partial x_j} - \frac{\partial u_j}{\partial x_i}\right). \tag{4.20}$$

This method uses the fact that Q has a positive value when vorticity is more predominant than shear strain. The condition also corresponds to the source term of the Poisson equation for the pressure ($\nabla^2 P = 2\rho Q$), so the condition shows that an area with Q $>$ 0 has the minimum pressure and is a local low-pressure area, and that a larger value of Q represents a stronger vortex. The Q-criterion is used for the investigation of flow structures in the wall jet zone. Figure 4.22 shows the coherent structures in an impinging jet. It is found that there is a strong acceleration and stretching of structures in this region. The positive Q values are very high, not only above the stagnation region, but also in wall jet region. This shows the strong vortical nature of the flow. The accelerating boundary layer flow in the radial wall jet experiences the entrainment of the surrounding cold fluid. This whole scenario results in reduction in wall temperature. This reduction in temperature is found to be significant from r/D$\approx$1 to r/D$\approx$2. However, after r/D>2 the boundary layer becomes thin due to radial spreading and reduction in velocity, due to this reason the wall temperature starts increasing again, which results in reduction in Nusselts number.

The Q surfaces colored by the magnitude of the turbulent kinetic energy are shown in figure 4.22. The regions of high turbulent kinetic energy coincides with the ring vortex impingement location on the wall. This shows that the ring vortex is affecting the flow field significantly. Lytle and Webb [131] attributed the occurrence of the secondary peak to the higher turbulence in boundary layer due to flow acceleration and intense shear between the radially ejecting jet and stagnant ambient. Also, the so-called *transition zone* (r/D =1 − 2) suggested by [159], where toroidal vortices and wall eddies developing and abruptly merging is in fact what was stated above. The Large Eddy Simulation confirms the previous experimental findings and it has been found that the seemingly different interpretations are the same.

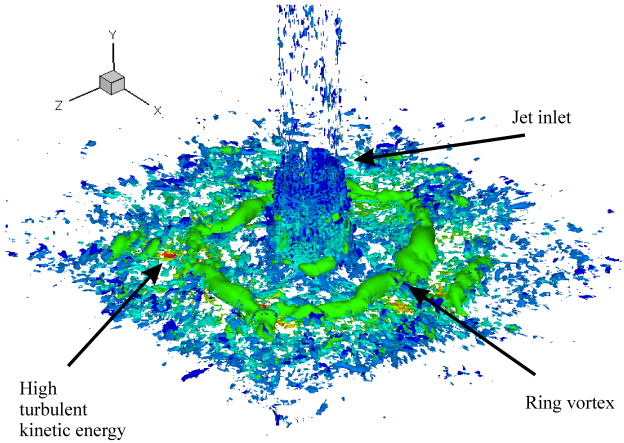

Figure 4.22: The $Q > 0$ surfaces (Q= $+3.15U_b^2/D^2$) in an impinging jet case. The Q surfaces are colored by turbulent kinetic energy. The red Q-surfaces are the zone of high turbulent kinetic energy which coincides with the ring vortex impingement zone.

4.2 LES of Jet Impingement with Active Velocity Field Excitation

It is known that through jet's velocity field excitation or pulsation, the jet behavior can be significantly altered. Pulsations affect not only the flow structures but also the entrainment effects. In the case of limited mass flow rate, the possibility of jet heat transfer enhancement is very important. In this section, the effect of excitation of fully developed turbulent impinging jet on heat transfer is investigated using LES. The jet is excited at four different frequencies, which correspond to a preferred mode, subharmonic and harmonic frequencies of the preferred mode of the un-excited jet. The amplitude of excitation is kept at 50 % of the inlet bulk velocity.

The inflow conditions are very important for the Large Eddy Simulation. For inflow conditions, the digital-filter based turbulence generation procedure proposed by Klein et al. [115] has been used. The mean velocity profile of fully developed turbulent flow is used for non excited jet. However, for the excited jet the inlet velocity field is altered based on the following relation:

$$U_{in} = U_b + A_N sin(2\pi ft) \tag{4.21}$$

where U_{in}, U_b and A_N are jet's inlet velocity, jet's bulk velocity and A is the amplitude of excitation. In this section it is taken as 50% of the U_b.

Computational Domain

A schematic representation of the computational domain is shown in figure 4.23. It consists of a circular impingement zone and a circular pipe of length 6D. The domain is confined by an adiabatic, no-slip wall at the top. Also the boundary condition at the pipe wall is made adiabatic and no-slip. The domain is 16D in length. The jet's Reynolds number, based on the time averaged bulk velocity U_b and jet's diameter D, is 23000. The dimensionless nozzle-to-plate distance (H/D) is 2. This domain and grid quality is same as used for the non-excited impinging jet simulation, which is investigated in the previous section.

In each case, the total simulation time is equivalent to 20 cycles, where one cycle corresponds to the preferred mode of unexcited jet.

Results

Figure 4.24 shows the energy spectrum of the velocity signal in case of excited and unexcited jet at the same position in the jet. Only the large scales are affected by the excitation and become more energetic. However the small scales are unaffected by the excitation. It is interesting to note that the slope of the spectrum is independent of the excitation. Experimentally, Azevedo et al. [11] have observed that the excitation only affect the large scale

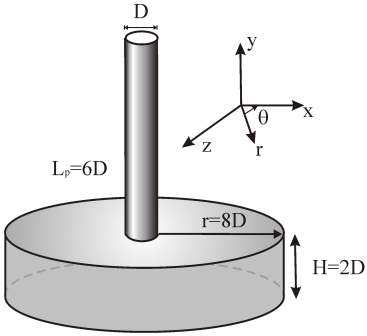

Figure 4.23: Schematic diagram of computational domain used for the impinging jet Large Eddy Simulation. The origin is fixed at the geometrical stagnation point of the jet.

structures. As the present simulations endorse these findings, the excited jet simulation on the same grid as used for non-excited jet is justified.

Instead of exciting the inlet velocity field at random frequencies, it is decided to excite the jet at frequencies corresponding to the jet's preferred mode (f_n), subharmonic of preferred mode ($f_{n/2}$), twice of preferred mode (f_{2n}) and five times of Preferred mode (f_{5n}). The Strouhal numbers of the jet are:

- St=0.16 (Naturally occurring subharmonic)
- St=0.32 (natural/preferred)
- St=0.6 (harmonic)
- St=1.45 (higher harmonic)

The instantaneous entrainment behavior at different excitational frequencies is shown in figure 4.25. Figure 4.26 shows the entrainment behavior in case of a natural jet. It is found that the fast change in velocity increases the structures renewal effect but it also makes the flow structures smaller, making them less effective for heat transfer enhancement.

Over the years, researchers with different objectives, investigated many interesting phenomena in excited jet cases, for example, large scale structural dynamics, vortex pairing, vortices collective interaction and unsteady separation of the wall boundary layer. In case of the excited jet impingement, the understanding of these phenomena is important, as they

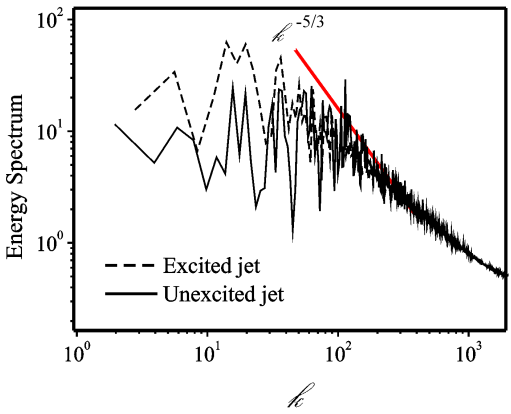

Figure 4.24: The turbulence spectrum in case of excited and unexcited jet.

may affect the heat transfer distribution on the target wall. It is therefore interesting to discuss the jet's flow field under excitation effects, which would help in understanding the differences between the heat transfer distributions discussed in this paper.

Kataoka et al. [109] have discovered the interesting phenomenon of surface renewal effects in case of impinging jets. According to them the flow over the target surface is renewed by the large scales structures depending on the H/D ratios, Reynolds number and velocity fluctuations. The large scale structures arise from the flow emerging from the nozzle and flow impact on the surface. These structures effect the whole flow field and control the impinging jet dynamics. The phenomenon in the stagnation zone is quantified through the surface renewal parameter, defined as:

$$Sr = \frac{\sqrt{(\overline{u'u'})_{stg}}}{U_{CL}} \frac{f_e D^2}{\nu} \tag{4.22}$$

where f_e is the frequency of the large scale structure passage frequency. It can be interpreted that the surface renewal parameter is the product of the turbulent Reynolds number and Strouhal number. Kataoka et al. [109] have found experimentally that as the surface renewal parameter increases the heat transfer on the target wall in the stagnation region increases. However, the investigations and reasoning proposed by Kataoka et al. [109] were valid

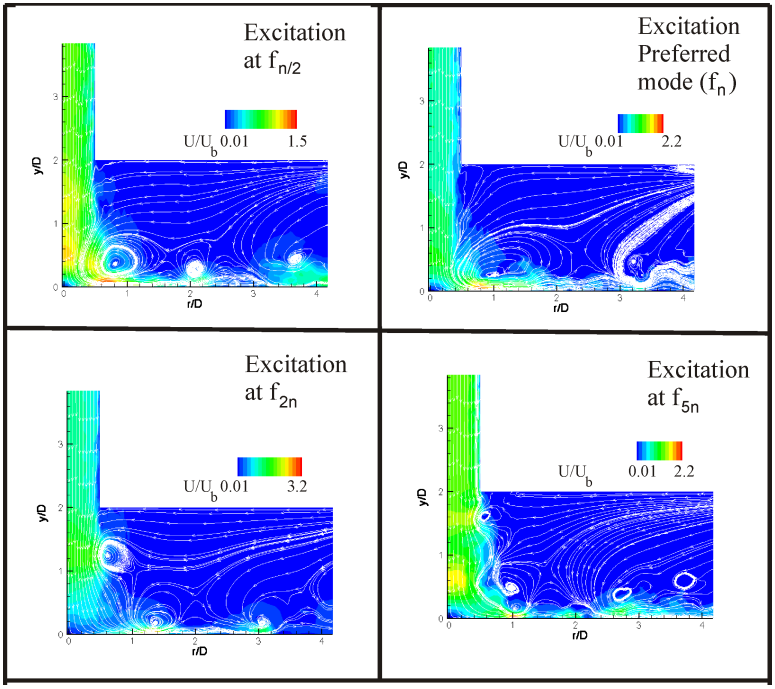

Figure 4.25: Instantaneous pathlines in case of jet inlet velocity excitation, at different time steps.

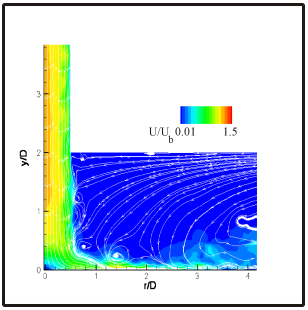

Figure 4.26: Instantaneous pathlines in case of unexcited (natural) jet.

only for the case of naturally occurring unexcited jet cases. However, as in case of jet excitation the turbulent coherent structures can be controlled it can be imagined that the surface renewal effect is controlled as well.

Another, important phenomenon in axisymmetric jets is vortex pairing in which two discrete vortices coalesce together. It can occur in free as well as impinging jets. Under controlled excitation multiple coherent structures merge together and it is called collective interaction [85]. Two of the characteristic features associated with the collective interaction are the sharp drop in passage frequency and relatively high shear-layer growth [84].

Several researchers have observed these phenomena in their experiments and its role in the heat transfer enhancement has been investigated (see [128; 53; 93]). In this investigations, in case of turbulent jet (Re=23000) at the amplitude of excitation of 50% with outlet-to-target wall distance (H/D) of two, no pairing and collective interaction pheomena could be observed. However, the phenomenon of unsteady separation is observed. Didden & Ho [38] have investigated the axisymmetric jet excitation at a Reynolds number of 19000 and the frequency of excitation corresponds to the preferred mode of the unforced jet. Landreth & Adrian [117] have investigated the impingement of a low Reynolds number turbulent circular jet using Particale Image Velocimetry (PIV). They found that the primary vortex or ring vortex causes the formation of secondary vortices at the wall, which are lifted away from the wall jet. Later both primary and secondary vortices merge together. A similar phenomenon has been observed through simulation. The sharp rise in the displacement thickness is an indication of unsteady separation. The displacement thickness is defined as:

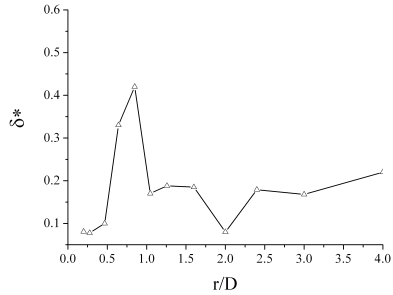

Figure 4.27: Displacement thickness (in mm) computed for wall jet boundary layer (excitation at preferred mode).

$$\delta^* = \int_0^{\delta} \left[1 - \left(\frac{u}{U_\infty}\right)\right] dy \tag{4.23}$$

where δ is the boundary layer thickness, U_∞ is the velocity at the edge of the wall jet boundary layer.

At one particular instant, figure 4.27 shows the displacement thickness at different radial

positions in case of excitation at the preferred mode. The sharp rise in the thickness is a sign of the unsteady separation. It is observed that in case of excitation at subharmonic frequency the unsteady separation is delayed.

The Anisotropy Invariant Map of turbulent stress tensor is plotted in figure 4.28. As described in section 4.1, in case of natural jet impingement the near wall turbulence at r/D=2 is following the axisymmetric contraction state but for y/D > 0.02, the turbulence is following the axisymmetric expansion state. This trend is also observed when jet is excited at $f_{n/2}$, f_n and f_{2n} frequencies. However, when jet is excited at higher harmonic frequencies the near wall turbulence follows the two-component state and then with out following the axisymmetric contraction it moves towards the axisymmetric expansion state. This shows that the nature of the turbulence in an impinging jet flow can be altered by the high frequency excitations.

The contours of turbulent kinetic energy for the excited and the unexcited jets, are shown in figure 4.29 and 4.30. In case of non-excited jet the turbulent kinetic energy is highest in the wall jet. The same trend can be seen in case of excitation at preferred mode and its subharmonic frequency. The change in trend is observed in case of excitation at frequencies higher than the preferred mode, the turbulent kinetic energy becomes higher more closer to the jet and later in case of higher harmonic excitation it is high at the jet outlet, with significant reduction in the amount of turbulent kinetic energy near the wall. Further, it is found that in case of natural jet the turbulent kinetic energy is concentrated at the location of the secondary peak. However, in case of excitation the turbulent kinetic energy is high in the wall jet zone but the distribution is uniform, causing the secondary peak to be flattened or removed.

The radial distribution of the Nusselt number in case of velocity field excitation is plotted in figure 4.31. The surface averaged Nusselt number & Nusselt number at the stagnation point under different excitation cases are plotted in figure 4.32 (a). The Nusselt number is plotted against Strouhal number of excitation. The semi-logarithmic plot of Nusselt number at the stagnation point versus Strouhal number is plotted in figure 4.32(b). The value of Nusselt number is normalized with the corresponding values of Nu in case of unexcited jet.

It is found that the excitation of inlet velocity field at high amplitude can improve the heat transfer. Although the heat transfer at the stagnation point is improved with the increase in excitational frequencies. The investigations at four different frequencies shows that the increase in surface averaged heat transfer is very significant at the frequency corresponding to the half of the preferred mode. It is interesting to note that the heat transfer can be enhanced with excitation of the inlet velocity field at the large amplitude (in our case 50%). However, care must be taken in selecting the excitational frequencies. The frequencies depend on the geometric configuration of the jet outlet, which in fact affects the jet flow instabilities growth and jet structure.

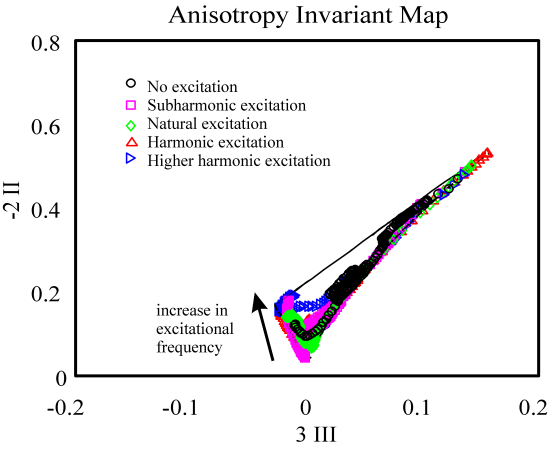

(a)

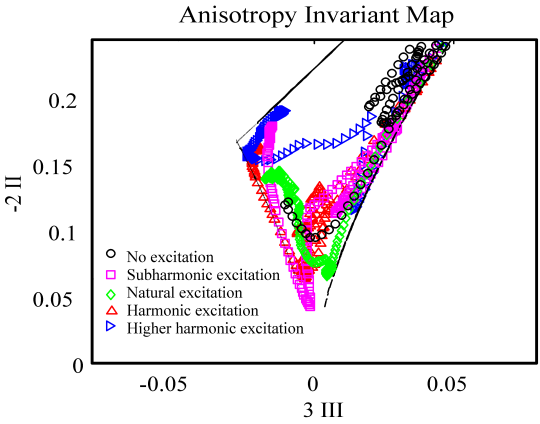

(b)

Figure 4.28: (a) Anisotropy Invariant Map (AIM) at r/D=2 with and with out inlet velocity field excitation (b) close up view.

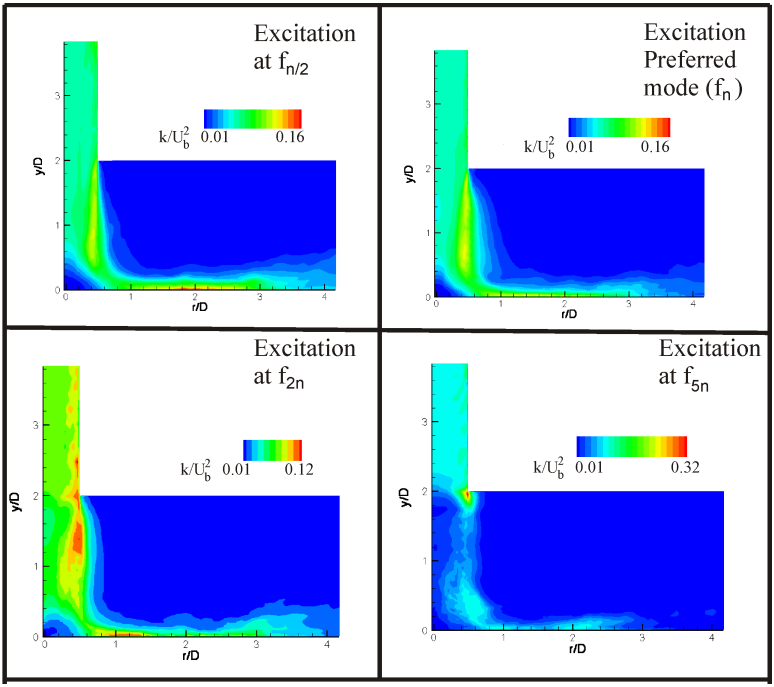

Figure 4.29: Turbulent kinetic energy in case of excitation.

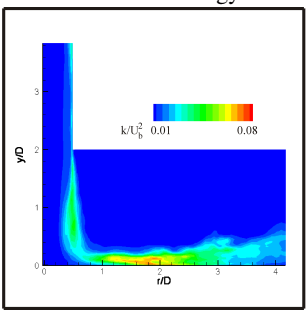

Figure 4.30: Turbulent kinetic energy in case of unexcited jet.

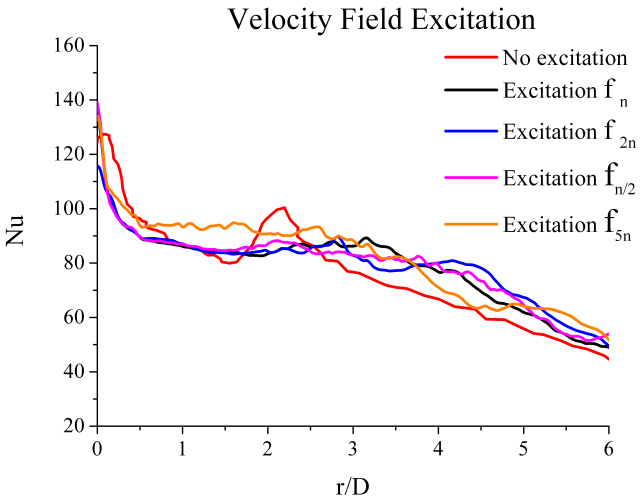

Figure 4.31: Radial distribution of Nusselt number in case of velocity field excitation.

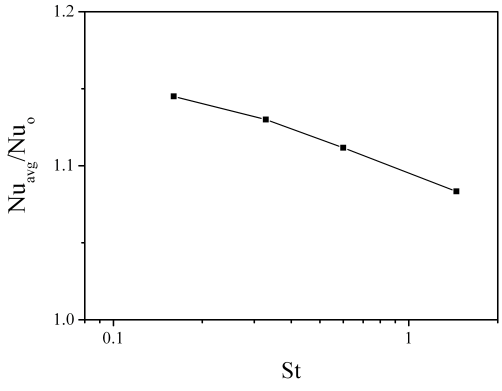

(a)

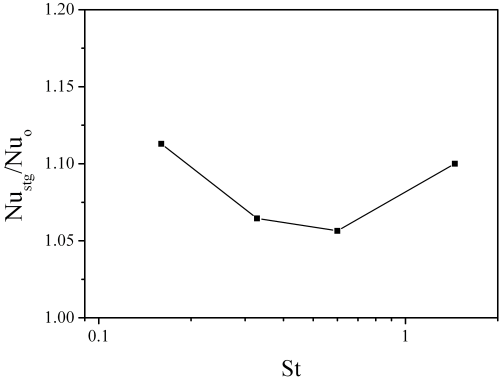

(b)

Figure 4.32: (a) The semi-logarithmic plot of surface averaged Nusselt number versus Strouhal number. (b) The semi-logarithmic plot of Nusselt number at stagnation point versus Strouhal number. The Nusselt number is normalized with the corresponding values of Nu in case of unexcited jet.

4.3 LES of Jet Impingement with Passive Velocity Field Excitation

Active control of excitations is an effective approach for heat transfer enhancement in an impinging jet. However, it demands efficiently designed mechanism for the control of the flow field. Passive excitation of the jet is a simple approach which can be accomplished by simple change in the geometry of the flow domain or by using some excitational devices. The devices of such kind are cylindrical inserts, rings, springs etc. In this section a case of passive excitation of the impinging jet's velocity field has been investigated. In the present investigation a cylindrical insert inside the pipe is modeled. The geometry of the computational domain is shown in figure 4.33 (a). The diameter of the cylindrical insert is half of the diameter of the main pipe. The center of the cylinder is at (x,y,z)=(0,2.2D,0) in Cartesian coordinates. The Reynolds number (Re=U_bD/ν) of the main pipe flow is 23000. The jet outlet-to-target wall distance is two.

Computational domain

The whole computational domain is modeled with an O-grid. At the impingement wall, the near wall grid fulfills the requirements of properly resolved Direct numerical simulations. The mean grid spacing near wall Δ^+/η^+ is 6.4, where η is the length of the Kolmogorov scale. The most important domain region is the stagnation and wall jet region (r/D$\leq$4), where the $\Delta r^+ = (\Delta r)u_\tau/\nu$ is $\approx$ 8 with in the jet zone and 16 in the wall jet region. The parameter $r\Delta\theta^+ = (r\Delta\theta)u_\tau/\nu \approx 20$. In the wall jet zone the maximum Δr^+ is 94. The grid near the cylindrical insert is finest, as the thin shear layer emanating from the cylinder and the subsequent wake region are the main flow features in this simulation. The grid spacing perpendicular to the cylinder are $\Delta_\perp^+$ = 0.5. Total 12 blocks are surrounding the cylindrical insert. Total 7.3 million control volumes are used for the simulation of this case.

The flow attains statistical stationary state after twenty cycles, where one cycle corresponds to the vortex shedding frequency of the cylindrical insert. Once the flow becomes statistical stationary, it is averaged in time and space. The simulation is controlled in such a way that the CFL number remains less than one. The dimensionless time step used is $\Delta t d/U_b$ equal to 3.57E-08, where d is the diameter of the cylinder. The total simulation time is equivalent to 90 cycles.

The computations were performed on the NEC-SX8 Cluster, Höchstleistungsrechenzentrum (HLRS), Stuttgart, Germany. The computations are done using 5 processors, using 33 blocks in total.

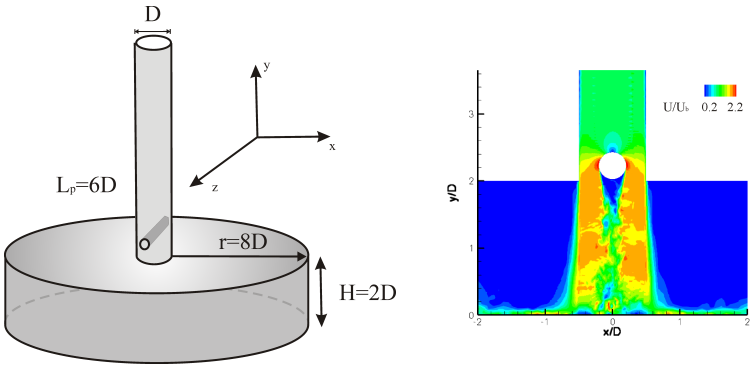

Figure 4.33: The schematic diagram of the computational domain used for the simulation of the passive jet excitation case.

Results

The instantaneous velocity field from the simulation is shown in figure 4.33 (b). As can be seen, the cylinder in the pipe causes the formation of the wake region which extends till the target wall. The size and strength of this wake region change in time and the vortices shed by the cylinder strike the surface.

Experimentally it has been found that different vortex structures form over the cylinder when free-stream flow passes over it. Different flow behavior according to the Reynolds number, based on the cylinder diameter and the free-stream velocity are outlined below [129].

In the LES investigations the Reynolds number of the flow the over the cylinder is 11500. However, the cylinder is inserted in a pipe (confined) and flow over it is far from free-stream conditions. No vortex street has been found, instead random turbulence has been found to be dominant in the wake region of the cylinder.

The velocity distribution at the pipe outlet with and without cylindrical insert is shown in figure 4.34(a). As can be noted the jet velocity is increased due to the cylindrical insert. Figure 4.34(b) shows the power spectral density of velocity fluctuations in the jet at y/D=1.

It is explained in section 4.1 that the velocity in wall jet, which forms after an impingement, does not exhibit the conventional law of the wall.

The following semi-logarithmic relation can be used to model the inner layer of the

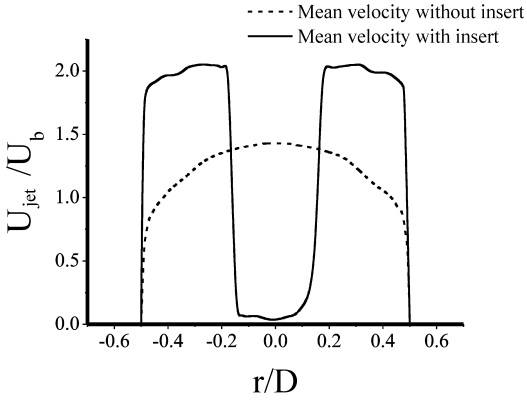

(a)

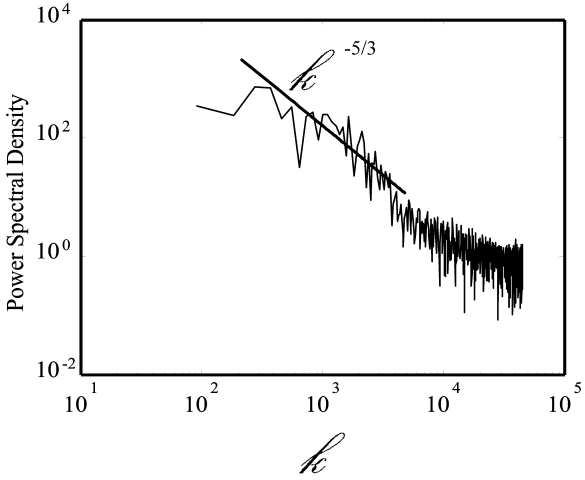

(b)

Figure 4.34: (a) The velocity distribution at the pipe outlet with and without insert. (b) PSD of velocity fluctuations in the jet at y/D=1, the line indicates the slope of the inertial subrange.

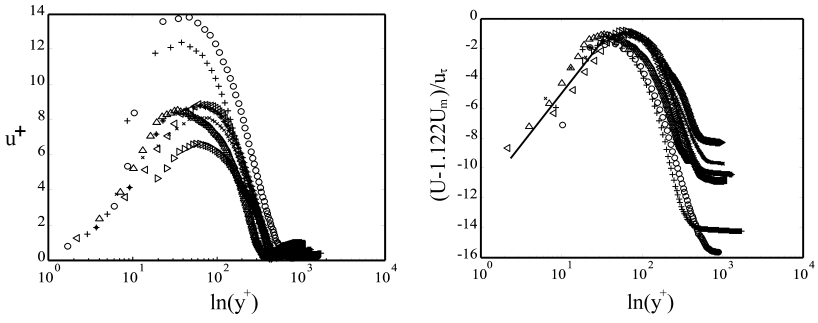

Figure 4.35: (a) Semilogarithmic plot of the radial velocity profiles with out subtracting the shift parameter, (b) Velocity profile with subtraction of profile shift parameter, the line shows the characteristic of the equilibrium layer that it extend till the location of maximum velocity.(Normal to the axis of insert)◯ r/D=1, + r/D=1.5, ∗ r/D=2, × r/D=2.5, ◁ r/D=3, ▷ r/D=3.5, △ r/D=4.

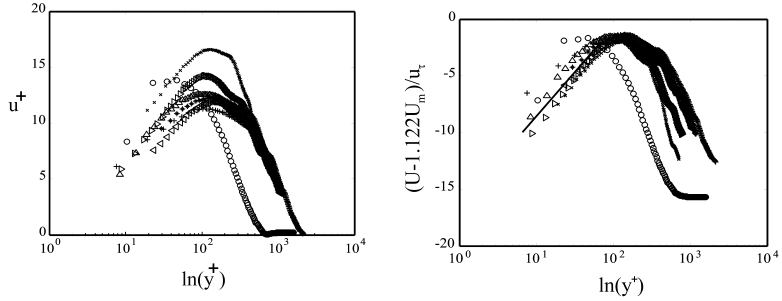

Figure 4.36: (a) Semilogarithmic plot of the radial velocity profiles with out subtracting the shift parameter, (b) Velocity profile with subtraction of profile shift parameter, the line shows the characteristic of the equilibrium layer that it extend till the location of maximum velocity. (Parallel to the axis of insert.)◯ r/D=1, + r/D=1.5, ∗ r/D=2, × r/D=2.5, ▷ r/D=3.5, △ r/D=4.

Table 4.1: **Flow over cylinder**

Reynolds number range	Flow over cylinder
$0 < Re_d < 5$	No flow separation
$5 < Re_d < 45$	Vortex pair attached to cylinder
$45 < Re_d < 200$	Purely laminar, vortex street
$200 < Re_d < 4.5\times 10^5$	Formation of vortex layer, Vortex street superimposed with irregular frequencies.
$Re_d > 4.5\times 10^5$	Turbulent vortex street

wall jet:

$$u^+ = \frac{u}{u_\tau} = \frac{1}{\kappa} ln(\frac{y u_\tau}{\nu}) + B \tag{4.24}$$

where u_τ is the friction velocity, κ is the von Karman constant and B is defined as:

$$B = f(\frac{U_m}{u_\tau}) \tag{4.25}$$

Using the approach proposed by [150; 63] the following relationship is obtained:

$$B = 1.122(\frac{U_m}{u_\tau}) - 10 \tag{4.26}$$

The first term in the above equation is called profile shift parameter, which is subtracted from the law of the wall, the resulting curve shows the presence of an equilibrium layer that extend up to the point of maximum velocity, as found for non-excited jet case. Figure 4.35(a) and 4.35(b) shows the radial velocity profiles with and with out subtracting the shift parameter in semi-logarithmic axes for the velocities normal to the insert axis in the wall jet direction. On the other hand, Figure 4.36(a) and 4.36(b) shows the radial velocity profiles with and with out subtracting the shift parameter in semi-logarithmic axes for the velocities parallel to the insert axis in the wall jet direction. As can be seen, close to stagnation point the velocities parallel to insert axis are deviated from the law of the wall. However, the value of B is found to be independent of the insert axis effect.

Figure 4.37 shows the distribution of turbulent kinetic energy in the cylindrical insert case. The kinetic energy is very high in the stagnation zone. Compared to no-insert case there is a 30% increase in the turbulent kinetic energy in the domain. The figure on the right hand side shows the close up view of the stagnation zone. Here the time averaged

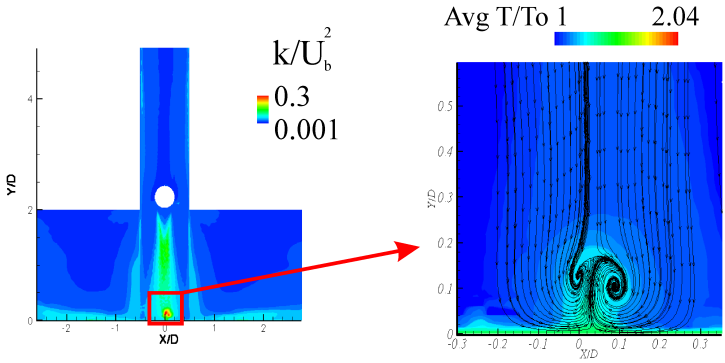

Figure 4.37: Distribution of turbulent kinetic energy. The figure on the right hand side shows the close up view of the stagnation zone.

streamlines are plotted. The contour shows the time averaged temperature field, which normalized by the jet's inlet temperature value. The target wall is heated with a constant heat-flux, therefore the flow there is hot. The flow coming from the cylindrical insert, sweeps the geometrical stagnation zone and an up-wash region is created. This complex flow dynamics has tremendous effects on the heat transfer distribution. It is found that under this highly complex flow field the heat transfer at the target wall is greatly enhanced. The time averaged and instantaneous radial distributions of the Nusselt number are plotted in figure 4.38 (a).

The fluctuations in the Nusselt number distribution are large in the wake region of the cylinder. However, as the wall jet develops the influence of the wake flow is reduced. Figure 4.38 (b) shows the radial distribution of the Nusselt number at the target wall compared to the case of no-cylindrical insert. Secondary peak in the radial distribution of the Nusselt number is found to be shifted towards the zone affected by the wake region. The impact of the high velocity jet streams, originated due to cylindrical insert, cause the increase in heat transfer. Lee et al. [121] have found that the Nusselt number at the stagnation point for a single jet impingement without insert, at H/D=2, can be related to $Re_D^{0.5}$. In the present case it is found that two jet streams emerged from the sides of the cylinder with velocity reaching twice as high as in the main pipe. This casues the Reynolds number to be doubled. Interestingly the Nusselt number at the stagnation is following the same trend as found for

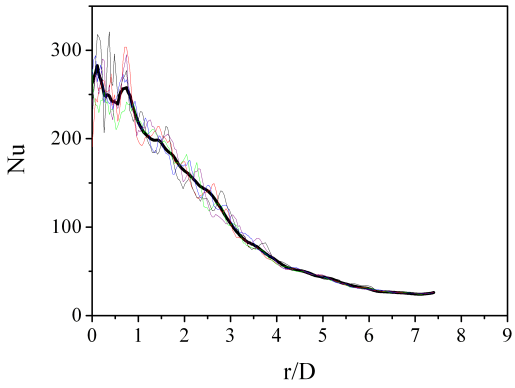

(a)

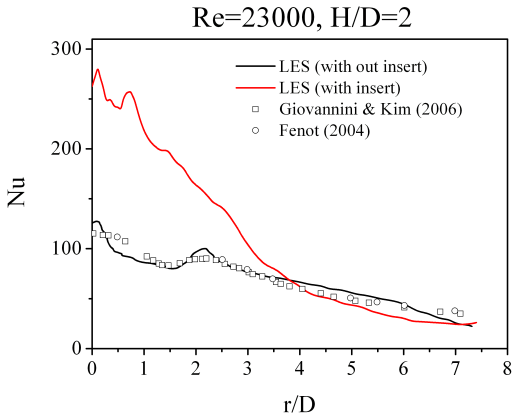

(b)

Figure 4.38: The instantaneous and time averaged radial distributions of Nusselt number. (b) The time averaged Nu distribution with and with out insert case.

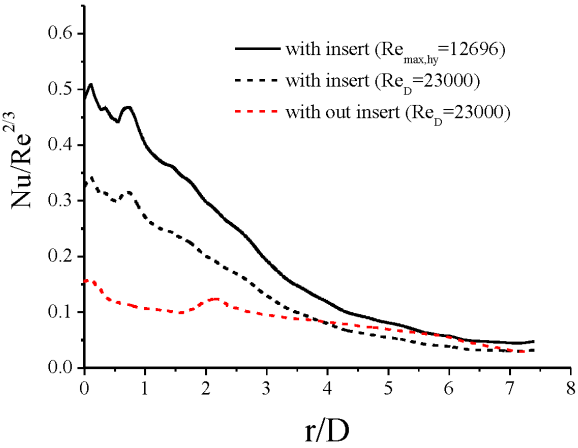

Figure 4.39: Radial distribution of Nusselt number normalised by $Re^{2/3}$.

jet with out insert case.

The radial distribution of Nusselt number normalised by $Re^{2/3}$ is plotted in figure 4.39. The Nusselt number is normalised by the Reynolds number of the flow in the main pipe. Also a new Reynolds number $Re_{max,hy} = U_{max}\ D_{hy}/\nu$ based on the jet's maximum velocity and the hydraullic diameter of the jet is used for the normalisation. As the effective flow area is reduced, the Reynolds number $Re_{max,hy}$ is smaller than the Reynolds number of the flow in the main pipe.

4.4 LES of Impinging Jet with Active Temperature Field Excitation

Introduction of controlled fluctuations in the inflow conditions of an impinging jet can significantly alter the heat transfer at the target wall. In this perspective, the investigation of the effect of changes in the jet's inlet temperature field on heat transfer is a pioneering investigation. In this section, the effect of an impinging jet's inlet temperature field excitation on heat transfer is investigated. The jet is excited at three different frequencies, which correspond to a preferred mode, subharmonic and harmonic frequencies of the preferred mode of the unexcited jet. The jet's inlet temperature field is excited according to the following relation:

$$T_{in} = T_b + A_N sin(2\pi ft) \tag{4.27}$$

where T_{in} and T_b are the jet's inlet and bulk temperatures respectively and A_N is the amplitude of excitation. In this thesis it is taken to be 50% of T_b, which corresponds to peak-to-peak $\pm$ 10^{o}C variation. The jet's Reynolds number, based on the bulk velocity U_b and jet's diameter D, is 23000. The dimensionless nozzle-to-plate distance (H/D) is 2. The computational domain and grid used are described in section 4.1.

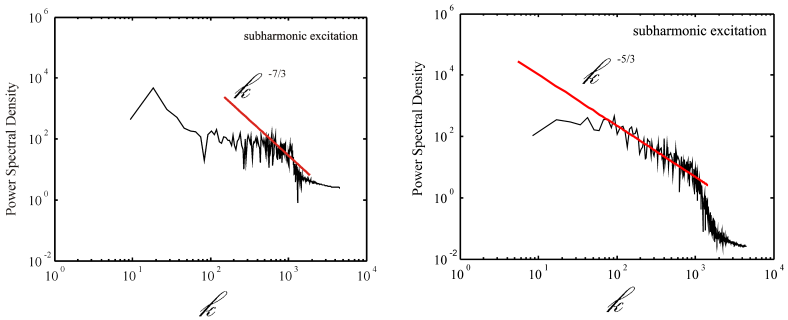

(a) (b)

Figure 4.40: Power Spectral Density of the (a) temperature fluctuations (b) velocity fluctuations inside the jet shear layer at subharmonic frequency.

Figure 4.42 shows the power spectral density of the temperature fluctuations inside the jet shear layer (y/D$\approx$ 1) when jet's inlet temperature field is excited at different frequencies. In each case, the slope of the spectrum in inertial range as shown by the line. The fluctuation

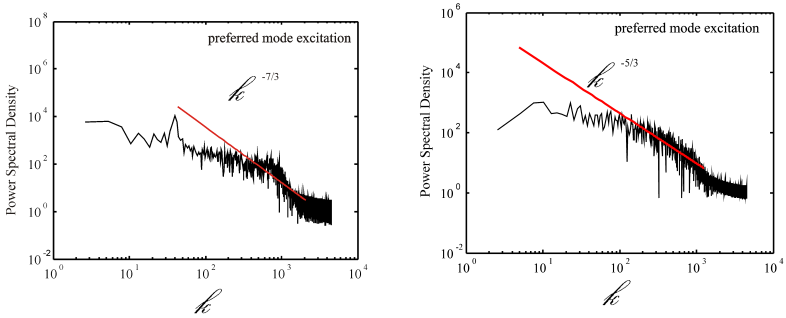

Figure 4.41: Power Spectral Density of the (a) temperature fluctuations (b) velocity fluctuations inside the jet shear layer at preferred mode.

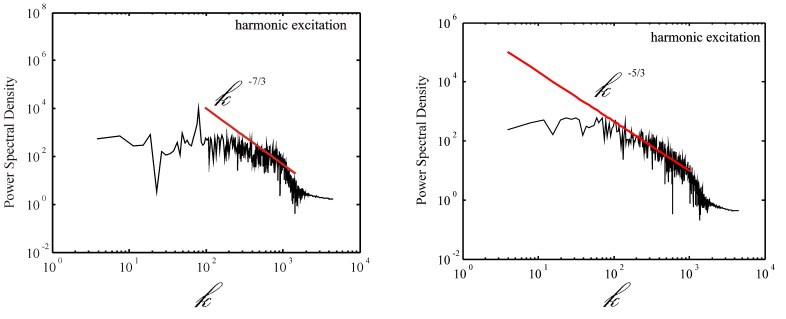

Figure 4.42: Power Spectral Density of the (a) temperature fluctuations (b) velocity fluctuations inside the jet shear layer at harmonic frequency.

in temperature signal exhibit the slope of -7/3. The prominent peaks corresponds to the excitational frequencies or wave numbers.

Thermal impact on the wall

The Nusselt number is defined as:

$$Nu = \frac{q_w}{(T_w - \overline{T_{in}})} \frac{D}{\lambda} \tag{4.28}$$

$\overline{T_{in}}$ is the time averaged jet's inlet temperature, which is equals to T_b= 293K. An important issue in case of temperature field excitation is the quantification of the thermal variation at the target wall. For that the instantaneous fluctuations in the Nusselt number are monitored at the target wall. Figure 4.43 shows the fluctuations in the instantaneous Nusselt number near the stagnation point (r/D=1.3) on the target wall, when the jet's temperature field is excited at three different frequencies. It is found that in case of subharmonic excitation the percentage difference between the maximum value of the Nusselt number and the time averaged value is around 87%. In case of excitation at preferred mode the percentage difference between the maximum value of Nusselt number and time averaged value is around 156%. In case of excitation at twice of the preferred mode, the percentage difference between the maximum value of Nusselt number and time averaged value is around 125%. This indicates that the subharmonic excitation are much better than other excitation cases.

Wall temperature fluctuations may cause cyclical thermal stresses and depending on the wall material may trigger fatigue cracking of the wall. The phenomenon is known as thermal striping. This can be analyzed by looking at the distribution of the crest factor (CF) or scalar variance at the target wall. Voke & Gao (1998) have used the crest factor to investigate the temperature variation on the target wall in case of hot jet impingement. The Crest factor is defined as:

$$CF = \frac{T_{max} - T_{min}}{T_{rms}} \tag{4.29}$$

It is found that in case of unexcited jet, the Crest factor is maximum in the wall jet zone at the location of r/D = 6. In the stagnation zone it is found to be less significant, which shows that the temperature fluctuations in this zone are small. The same conclusion has been drawn from the estimation of the scalar variance, therefore only the scalar variance has been used for the quantification of the thermal impact in case of excited jets. The scalar variance $\overline{T'T'}$ quantify the effect of the fluctuation in the temperature field.

Radial distribution of Nusselt number in case of temperature field excitation is shown in figure 4.46. The excitation will affect the Nusselt number till r/D<3. After that although

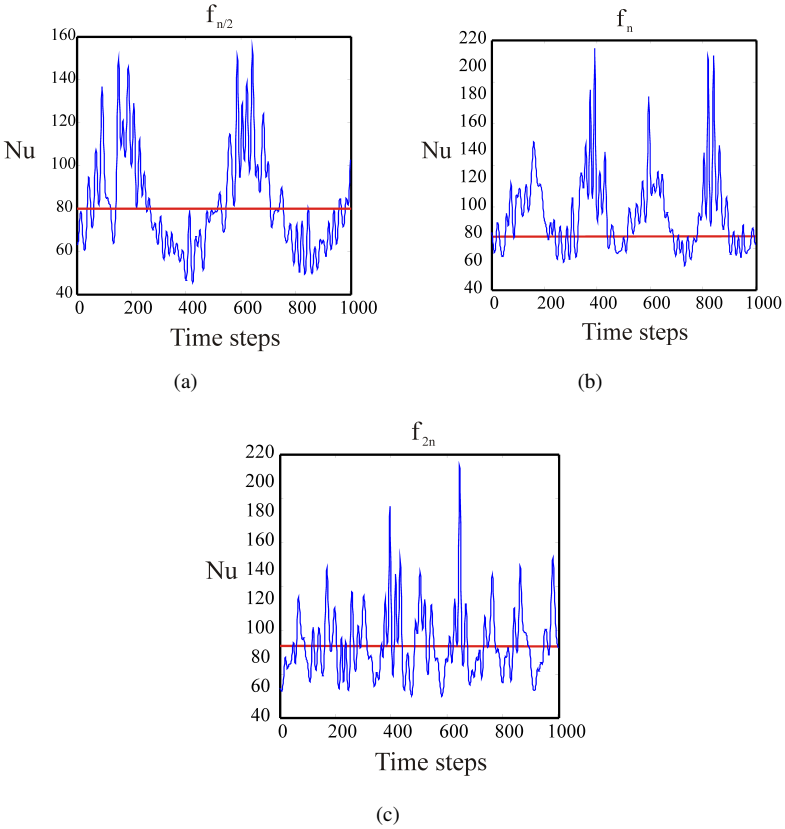

Figure 4.43: Fluctuations in the Nusselt number at the target wall near stagnation point (r/D=1.3) when jet temperature field is excited at (a) subharmonic frequency (b) preferred mode (c) harmonic excitations. The red line shows the time averaged value.

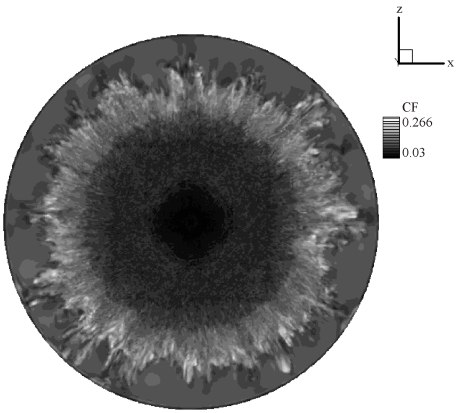

Figure 4.44: Contour plot of crest factor on the target wall (with out excitation).

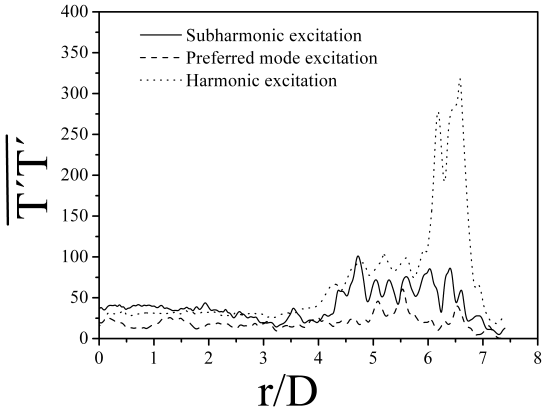

Figure 4.45: Radial distribution of scalar variance at the target wall in case of temperature excitation.

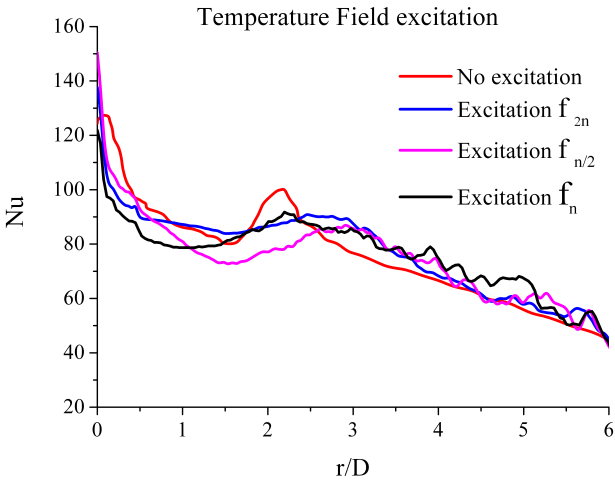

Figure 4.46: Radial distribution of Nusselt number in case of temperature field excitation.

the heat transfer due to excitation is higher than the non-excitation case, the time averaged Nusselt number distribution exhibit a random character.

It is interesting to note that the radial distribution of the Nusselt numbe is very different from the natural jet impingement case. Excitation of the temperature field at subharmonic frequency is found to be the most promising technique for heat transfer enhancement at stagnation point. However, in case of excitation at higher harmonic frequencies, the risk of faliure is high. In case of excitation at preferred mode, the surface-averaged Nusselt number is higher than the other cases.

4.5 LES of Swirling Jet Impingement

Swirling jets consist of complex flow features like, spiral type flow instabilities, vortex breakdown and free shear layer. The control of these features through different swirling rates and their influence on the heat transfer at the target wall is an interesting inquiry. In this section, the results of the Large Eddy Simulations of a swirling jet impingement at the Reynolds number (Re=U_{ax}D/ν) of 23000 and 21000 are presented. The jet outlet-to-target wall distance (H/D) is two. The swirl number of the jet are 0.2, 0.39 and 0.47. The heat transfer due to swirling jet is compared with the experimental findings of Yan & Saniei [195].

In order to understand the influence of different parameter on the heat transfer due to swirling jet the swirl number, Reynolds number and the jet's inlet temperature is varied as tabulated below.

Table 4.2: **Large Eddy Simulations**

Cases	Swirl	Re	Jet Inlet Temperature
Case-I	0.47	23000	300 K
Case-II	0.2	23000	293 K
Case- III	0.5	21000	298 K
Case- IV	0.39	21000	293 K

Swirling Jet Inflow Conditions

For the numerical simulation the precursor simulation of rotating pipe flow is used by some researchers. However, generating inflow through such a procedure is time consuming and demands extra computational cost. The specification of inlet velocities based on the expressions of forced vortex and Rankine vortex are also used. However, they are too simplified and usually do not give good quality results. In the experiment of Yan and Saniei [195], the swirl is imparted to the fully developed turbulent pipe flow by tangential jets. The same procedure is used here. The tangential velocity is superimposed on the fully developed pipe flow. The turbulent fully developed flow is prescribed in axial direction and described above for the non-swirling jet case.

The mean tangential velocity prescribed through an empirical relation is plotted in Fig. 4.49. The empirical relation is reported by [97]:

$$\frac{u_\theta}{u_\theta^*} = \left[\frac{2\vartheta}{1+\vartheta^2}\right]^{\kappa^*} \tag{4.30}$$

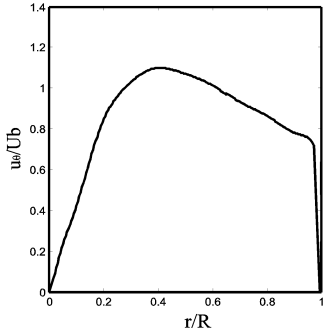

Figure 4.47: Distribution of the tangential velocity (Re=23000, S=0.47).

where, $\vartheta = r/r^*$, $r^* = 0.51\ \mathrm{R}\ \phi_*^{0.41}$, $u_\theta^* = 2.04\ u_{ax}\ \phi_*^{1.1}$. Here κ^* is an index depending on the swirl conditions and R is the radius at the jet outlet. The parameter ϕ_* is comprised of swirl number and axial momentum flux S/G_{ax} .

Problem Description & Computational Setup

Fig. 4.48 shows the schematic representation of the domain used for the investigation of the heat transfer due to impingement of the swirling jet at a bulk Reynolds number of 23000. First the swirling jet is simulated using the same computational domain as used for non-swirling jet simulation. However, this causes the swirl rate decay in the pipe, therefore, a different domain is utilized for the swirling jet investigation. The grid spacing in dimensionless units is $\Delta r^+ \approx 27$, $r\Delta\theta^+ \approx 20$ and $\Delta y^+/\eta^+$ is 6, where, η is the length of the Kolmogorov scale. In the investigations, a hexahedral structured grid has been used. The heat flux of 1000 W/m^2 is applied at the impingement wall. Total 6.4 million control volumes are used for the simulation of this case.

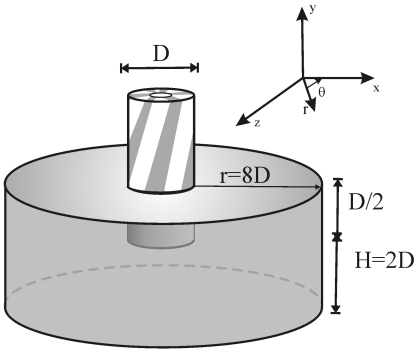

Figure 4.48: Schematic diagram of the computational domain used for swirling jet. The origin is fixed at the geometric stagnation point. The jet enters at y=2D. A swirling device is shown for clarification but not modeled.

Solution Control

On average total simulation time for each case is equivalent to 20 cycles, where one cycle corresponds to the natural frequency of non-swirling jet. The flow becomes statistical stationary after about 9.3 cycles. The simulation is controlled in such a way that the CFL number remains less than one. The dimensionless time step used is $\Delta t D/U_{ax}$ equal to 7E-07.

Computations are done on two different computing clusters available at Höchstleistungsrechenzentrum (HLRS), Stuttgart, Germany. For Case-I, the vectorized version of the code is used and computations are done on NEC-SX8 cluster. Case II, III and IV are computed on CRAY Opteron Cluster.

Result

Case-I

Due to the addition of a swirl the jet breaks down before impingement. At small swirl number, the jet's breakdown is delayed, on the other hand, at high swirl values it is enhanced. The complexity of the flow field can be visualised through iso-velocity surfaces, shown in figure 4.49. The phenomenon of the swirling jet impingement is different from the non-swirling jet impingement in a number of ways. Figure 4.49 shows the contour of instantaneous velocity distribution and Fig. 4.50 shows the distribution of turbulent kinetic

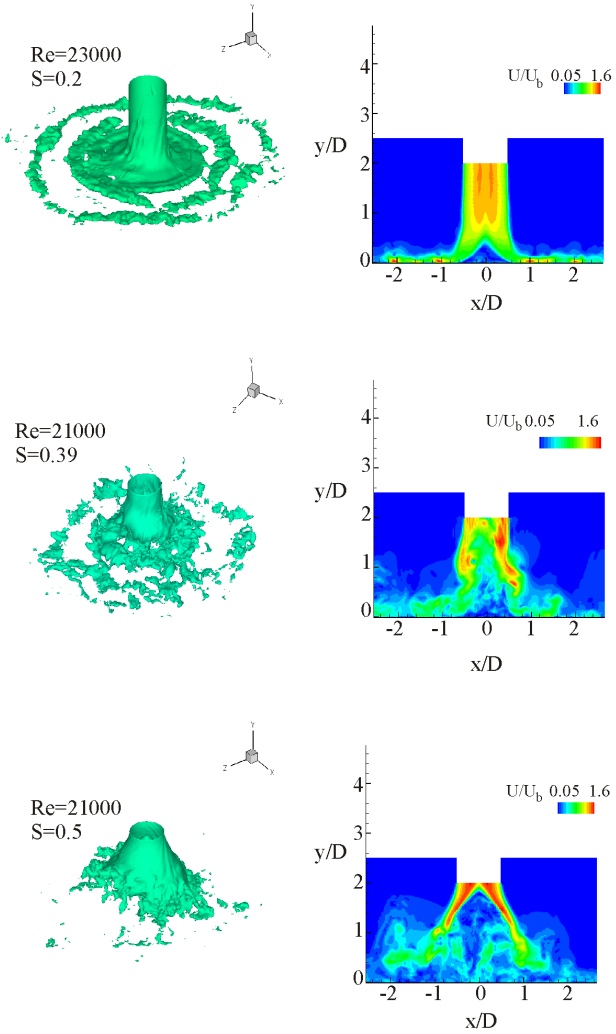

Figure 4.49: The iso-velocity surfaces (U/U_b=0.77) and instantaneous velocity field contours in the swirling jet domain.

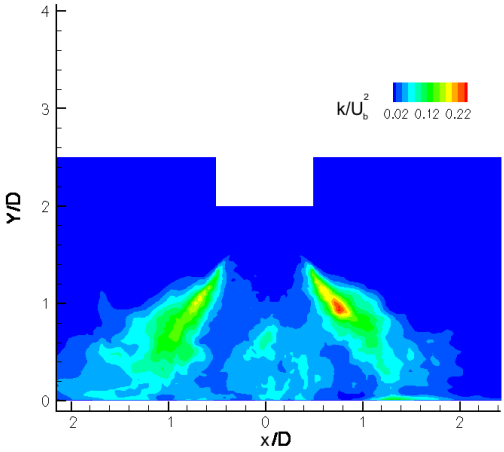

Figure 4.50: The contours of turbulent kinetic energy in the swirling jet (Re=23000, S=0.47).

energy in the swirling jet. As as be seen, the turbulent kinetic energy reaches its maximum at H/D=1. In case of the non-swirling jet the maximum in turbulent kinetic energy is found to occur close to the wall. In case of the non-swirling jet, the peak value of the Nusselt number occurs at the geometric stagnation point. On the other hand, in case of the swirling jet, the swirl causes the jet break down before the impingement and causes the formation of the several impingement zones at the target wall. A strong recirculation zone forms at the geometric stagnation location. The flow in this zone is heated causing a heat transfer reduction.

The Nusselt number distribution is defined as:

$$Nu = \left(\frac{q''_w}{T_w - T_j} \right) \frac{D}{\lambda} \tag{4.31}$$

where, q''_w is the heat flux at the target wall. T_w is the temperature attained by target wall after jet impingement and T_j is the jet's inlet temperature.

Figure 4.51 shows the radial distribution of the Nusselt number.

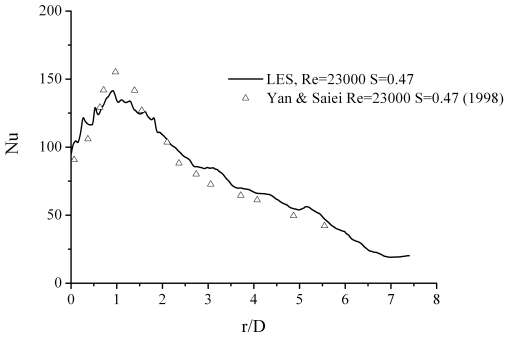

Figure 4.51: Radial distribution of the Nusselt number case of swirling jet impingement (Re=23000, S=0.47).

The result is in very good agreement with the experimental data of Yan and Saniei [195]. The case is used for a benchmark testing of the LES set-up.

Case-II

Recently, Lee et al. [123] and Yan and Saniei [195] have reported separately the heat transfer distribution due to swirl at Re of 23000 and S=0.2 at H/D = 2 case. However the reported Nusselt number distribution trends were not only different in trends but are enormously high. According to Yan and Saniei [195] the anomaly is hard to explain. Therefore, the need to investigate this case in detail is clear. The Nusselt number distribution predicted is compared with the experimental data. The radial distribution of the Nusselt number follows the trend of the Nusselt number distribution obtained in Case-II. Figure 4.52 shows the distribution of the Nusselt number for this case.

The radial distribution of the Nusselt number has been further checked by computing the surface averaged Nusselt number, defined as:

$$\overline{Nu} = \frac{1}{A}\int_A NudA \tag{4.32}$$

The surface averaged Nusselt number obtained from LES is compared with the empiri-

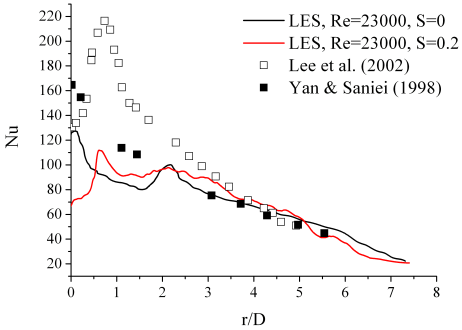

Figure 4.52: Radial distribution of the Nusselt number in case of swirling jet impingement (Re=23000, S=0.2).

cal correlation proposed by Ward and Mahmood [188]:

$$\overline{Nu} = CRe^{0.8}Pr^{0.33}(H/D)^{-0.2}(1-S)^{0.57} \tag{4.33}$$

The correlation is valid for the condition of $S < 0.48$ & H/D = 2 - 12, where, C is taken as C=0.032 till r/D=6.5.

The percentage difference between LES and Ward& Mahmood correlation is around 7%.

Case-III & IV

Radial distribution of the Nusselt number due to swirling jet at Reynolds number of 21000 and swirl of 0.39 and 0.5 is plotted in figure 4.53. The jet's inlet temperature is different in both cases. It is found that the higher jet inlet temperature results in the higher Nusselt number. Further, the increase in swirl increases the jet spreading rate. Due to this the jet impingement also shifts. In general, it has been found that the addition of the swirl does not give any appreciable increase in heat transfer for the H/D=2 case.

Swirling Jet Kinematics and Heat Transfer

Figure 4.54 shows the coherent structures extracted through iso-vorticity surfaces (ω_y) under different Reynolds number and swirl levels. The figure shows that at small swirl level

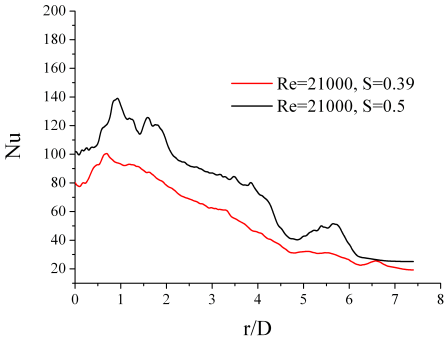

Figure 4.53: Radial distribution of the Nusselt number in case of swirling jet impingement (Re=21000, S=0.39 & 0.5).

the jet core is behaving like a rotating solid body. As the swirl increases the jet core exhibit helical shaped structures but their influence to the heat transfer at the wall is limited.

Senda et al. [172] have found that the location of the peak value in the radial distribution of the Nusselt number correlates strongly with the approaching maximum velocity near the wall. Abrantes and Azevedo [5] have discovered that turbulent kinetic energy can also be correlated with the peak value in the radial distribution of the Nusselt number. Through the simulation it is found that in case of high swirl number jet, the peak value in radial distribution of the Nusselt number is better correlated with the occurrence of maximum turbulent kinetic energy close to the wall. However at small swirl number the peak value in the radial distribution of the Nusselt number is correlated with the approaching velocity.

Table 4.3: **Location at the target wall (r/D)**

Re	S	$P_{k_{max}}$	$P_{k_{min}}$	k_{max}	Nu_{max}	U_m
23000	0.2	1.38	1.92	1.93	0.644	0.52
21000	0.39	0.68	1.0	0.8	0.66	1
21000	0.5	0.66	0.71	0.8	0.90	1.2

Table 4.3 outlines the locations (r/D) at the wall where the said quantities appear. For

example in case of jet's Reynolds number 21000 and swirl number 0.5, the maximum value of the production of turbulent kinetic energy occurs at r/D=0.66, the minimum value of the production of turbulent kinetic energy occurs at r/D=0.71, the maximum value of turbulent kinetic energy occurs at r/D=0.8. Similarly the maximum value of the Nusselt number occurs at r/D=0.90 and the maximum value of the velocity approaching the target wall occurs at r/D= 1.2. This shows that there exist strong correlation between the turbulent kinetic energy and Nusselt number. It can be inferred from the information presented in table 4.3 that at small swirl numbers the jet velocity approaching the target wall plays an important role in control of heat transfer. However, as the swirl increases the turbulent kinetic energy is found to play an important role. LES thus confirms the result of Senda et al. but found to be valid at small swirl numbers (S=0.2). Correlation between turbulent kinetic energy and Nusselt number is found to be strong when swirl number is high (S=0.39, 0.5).

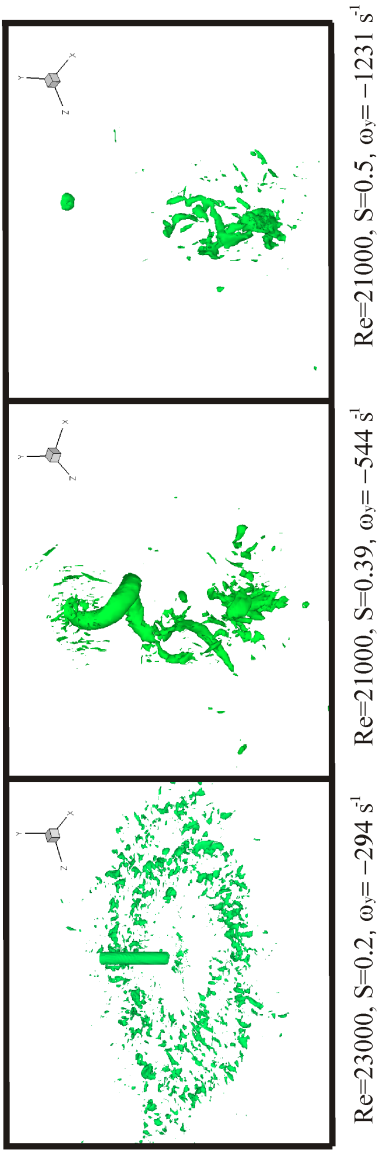

Figure 4.54: Coherent structures extracted through iso-vorticity surfaces.

5. AN ASSESSMENT OF SCALAR-FLUX MODELING FOR COMPLEX FLOWS

The computation of turbulent flows in problems of engineering interest often demands the investigation of flow at high Reynolds numbers. Such flows under computing memory and time constraints can only be simulated through Reynolds Averaged Navier-Stokes equations (RANS) based turbulence models. Therefore, the RANS based turbulence models are constantly being refined and improved. In the analysis of problems of industrial significance, the need to model complex flows with higher accuracy and certainty is urgent. The mean deformation rates in simple flows are usually mild and turbulence has time to achieve an equilibrium state with the mean flow. Because of this reason, the principal directions of the Reynold stress tensor tend to be aligned with those of mean strain and an eddy-viscosity representation of turbulence, used in some turbulence models, is adequate. However, in complex flows the principal axes of the Reynolds stress tensor are not aligned with those of the mean deformation tensor, as they involve extra strain rates which are absent in classical boundary layers.

In the engineering analysis, not only the correct prediction of momentum field is important but also the heat transfer might be important. The traditional approach for the convective heat transfer computation is based on the concept of the turbulent Prandtl number. According to this approach the turbulent scalar-fluxes are approximated using Fourier's law:

$$-\overline{u_i' T'} = \Gamma_t \frac{\partial T}{\partial x_i} \tag{5.1}$$

where, Γ_t is called eddy thermal diffusivity related to turbulent Prandtl number and momentum diffusivity as:

$$\Gamma_t = \nu_t / Pr_t \tag{5.2}$$

The turbulent Prandtl number which is often taken as a constant is in fact a variable dependent on the Reynolds stresses, turbulent heat flux and mean temperature and velocity gradients. Kasagi et al. [107] have done a Direct Numerical Simulation (DNS) of passive scalar field in turbulent channel flow. They found that the turbulent Prandtl number is a

varying quantity. Also the arguments usually stated for the justification of this approach are valid for fluids with molecular Prandtl number close to unity only. Jischa and Rieke [102] have found that the Pr_t is a weak function of the molecular Prandtl number for fluids having Prandtl number greater than one. However, the turbulent Prandtl number increases rapidly as Prandtl number reduces.

Due to this reason researchers have proposed non-linear, algebraic transport equations models for the computation of convective heat transfer.

The exact transport equation for the turbulent scalar flux vector can be written as (see [199]):

$$\begin{aligned}\frac{D\overline{u_i'T'}}{Dt} = & \underbrace{-\overline{u_i'u_j'}\frac{\partial T}{\partial x_j} - \overline{u_j'T'}\frac{\partial U_i}{\partial x_j}}_{P_{Ti}} \\ & \underbrace{-\frac{\overline{p'}}{\rho}\frac{\partial T'}{\partial x_i}}_{\Pi_{Ti}} \\ & \underbrace{-\nu\left(1+\frac{1}{Pr}\right)\overline{\frac{\partial u_i'}{\partial x_j}\frac{\partial T'}{\partial x_j}}}_{\varepsilon_{Ti}} \\ & \underbrace{-\frac{\partial}{\partial x_j}\left(-\nu\overline{T'\frac{\partial u_i'}{\partial x_j}} - \gamma\overline{u_i'\frac{\partial T'}{\partial x_j}} + \overline{u_i'u_j'T'} + \overline{\frac{T'p'}{\rho}}\delta_{ij}\right)}_{D_{Ti}}\end{aligned} \tag{5.3}$$

where, D_{Ti} is the molecular and turbulent diffusion, P_{Ti} is the production term, Π_{Ti} is pressure scalar gradient correlation, ε_{Ti} is destruction rate tensor. Also, γ, ν, ρ and Pr are molecular thermal diffusivity, momentum diffusivity, density and Prandtl number respectively.

As one can see, the equation represents a detailed description of turbulence scalar flux transport. However, as usually the case with the RANS based modeling, because of averaging, the information has been lost and solution requires an input from the user side. Instead of computing the equation 5.3, equivalent explicit algebraic scalar flux models (ESFM) are offered by numerous researchers, like Daly and Harlow (1970) [32], Rogers, Mansour and Reynolds (1989) [163], So and Sommer (1996) [174], Suga and Abe (1999)[180], Abe and Suga (2001) [2] and Younis, Speziale and Clark [199]. The commonly used models are:

Daly and Harlow (1970) suggested the relation [32]:

$$-\overline{u_i' T'} = C_{\theta 1} \frac{k}{\varepsilon} \overline{u_i' u_j'} \frac{\partial T}{\partial x_j} \tag{5.4}$$

where $C_{\theta 1}$ = 0.3.
Abe and Suga (2001) have proposed the relation [2]:

$$-\overline{u_i' T'} = C_{\theta 2} \frac{k}{\varepsilon} \overline{u_i' u_k'} \frac{\overline{u_k' u_j'}}{k} \frac{\partial T}{\partial x_j} \tag{5.5}$$

where $C_{\theta 2}$ is 0.6.
Younis, Speziale and Clark (2005) have proposed the model [199]:

$$\begin{aligned} -\overline{u_i' T'} = C_1 \frac{k^2}{\varepsilon} \frac{\partial T}{\partial x_i} + C_2 \frac{k}{\varepsilon} \overline{u_i' u_j'} \frac{\partial T}{\partial x_j} + C_3 \frac{k^3}{\varepsilon^2} \frac{\partial U_i}{\partial x_j} \frac{\partial T}{\partial x_j} \\ + C_4 \frac{k^2}{\varepsilon^2} \left(\overline{u_i' u_k'} \frac{\partial U_j}{\partial x_k} + \overline{u_j' u_k'} \frac{\partial U_i}{\partial x_k} \right) \frac{\partial T}{\partial x_j} \end{aligned} \tag{5.6}$$

where the coefficients are C_1 = -0.0455, C_2 = 0.373, C_3 = -0.00373, C_4 = -0.0235. For near-wall turbulent flows the model is further adjusted by including parameters that are sensitive to changes in turbulence structure in the near wall region. These parameters are the turbulent Reynolds number (Re_t), turbulent Peclet number (Pe_t), second and third invariants of the Reynolds stress anisotropy tensor (A_{ij}) and the stress flatness parameter (A). The Re_t is a scalar quantity which represents the ratio of the turbulent to molecular shear stresses and its value tends to zero at the wall. Near the wall, the anisotropy of the flow is very important which is included by tensors A_{ij}. It has been found that the coefficient C_1 has a smaller value than earlier reported. The recent recommendation for C_1 is given in the form of a damping function [200]:

$$C_1^* = C_1 [1 - exp(-A\beta Pe_t^{\alpha})] \tag{5.7}$$

where,

$$Pe_t = Re_t Pr$$

$$Re_t = \frac{k^2}{\nu\varepsilon}$$

$$A_{ij} = \frac{\overline{u_i' u_j'}}{k} - \frac{2}{3}\delta_{ij}$$
$$A_2 = A_{ij}A_{ij}$$
$$A_3 = A_{ij}A_{jk}A_{ki}$$
$$A = 1 - \frac{9(A_2 - A_3)}{8}$$

The new coefficients α and β, recommended for the C_1 modification, are 0.1 and 1.5 respectively. The values for α and β have been determined via DNS data of wall-bounded flows. However, there is still a need to assess the coefficients for more complex flows.

The coefficients of these ESFM are meticulously calibrated by investigators, but often for the cases of simple channel flows. Wikström et al. [192] (2000) used DNS data of channel flows. Abe and Suga [2](2001) and Younis et al. [199] (2005) used LES data of channel flows. There still is the need for analysis and reassessing the model for cases of more complex flows, like jet impingement or flow separation.

Recently impinging jets have been simulated via LES by a number of researchers like Gao and Leslie (1995), Gao and Voke (1995) [55; 56], Olsson and Fuchs (1998) [149], Cizesla et al. [30; 31], Tsubokura et al. [183], Hadžiabdić and Hällqvist have reported separately the investigation of impinging jet case using LES [78; 79]. In general, it is found that LES is a powerful tool for complex flows simulations. Recently, Abe [3] (2006) has used LES data for a plane impinging jet, with flow Reynolds number of 6000 and nozzle-to-plate spacing of 10, for the calibration of the coefficients of a *quadratic* model.

Originally, the coefficients of the Younis et al. explicit scalar flux model (ESFM) were calibrated using homogeneous turbulence data. Later, the model was refined for complex turbulent channel flows and modified parameters were introduced.

In this chapter, the coefficients of the scalar-flux models are investigated using the LES data of a natural jet impingement case reported in section 4.1. An important inquiry, in an impinging jet, is the distribution of the $\overline{u_r' T'}$, $\overline{u_\theta' T'}$ and $\overline{u_y' T'}$ in the wall jet zone, which is disscused in the next section.

5.1 Turbulent Heat Flux Distribution

The distribution of dimensionless turbulent heat fluxes at two different locations are shown in figure 5.1. The locations selected are r/D=0.5 and 2, i.e one close to the stagnation zone and the other in the wall jet zone close to the secondary maximum in the radial distribution of the Nusselt number. Close to the wall, the dimensionless radial turbulent heat flux has

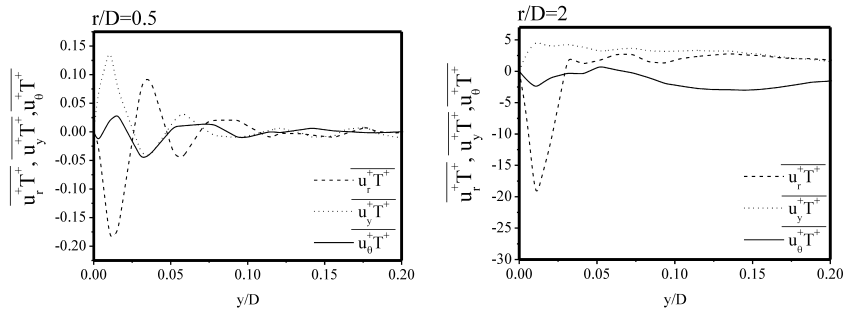

Figure 5.1: Distribution of $\overline{u_r'T'}$, $\overline{u_\theta'T'}$ and $\overline{u_y'T'}$ obtained from LES at r/D=0.5 (a), 2 (b). The distributions are normalised by frictional velocity at pipe wall and temperature $q_w/\rho c_p u_\tau$.

dominating effect. However away from the wall, at $y/D\approx$0.05 the order of magnitude is same as that of dimensionless azimuthal heat flux. Further at, $y/D\approx$0.2, all the turbulent heat fluxes have the same order of magnitude. It is interesting to note that the wall temperature increases as the wall jet region develops, as boundary layer becomes thin, which causes the increase in heat-flux.

Assuming, a two dimensional boundary layer, the turbulent Prandtl number is defined as:

$$Pr_t = \frac{\overline{u_r'u_y'}\frac{\partial T}{\partial y}}{\overline{u_y'T'}\frac{\partial U}{\partial y}} \tag{5.8}$$

Using LES data, the turbulent Prandtl number is computed at three different radial locations in the wall jet zone. Figure 5.2 shows the distribution of the turbulent Prandtl number in wall normal direction. As for a channel flow, it is found that near the wall the turbulent Prandtl number reaches a constant value. However, near the wall, as the wall jet region develops the turbulent Prandtl number changes as well.

One can expect that the turbulence models using constant turbulent Prandtl number might not perform well for impinging jet case. Behnia et al. [14] have investigated the effect of turbulent Prandtl number variation on the prediction of turbulent impinging jet heat transfer using the υ^2-f model. Three different constant turbulent Prandtl numbers (Pr_t=0.73, 0.85 and 0.92) along with experimental data reported by [111] were compared. For this

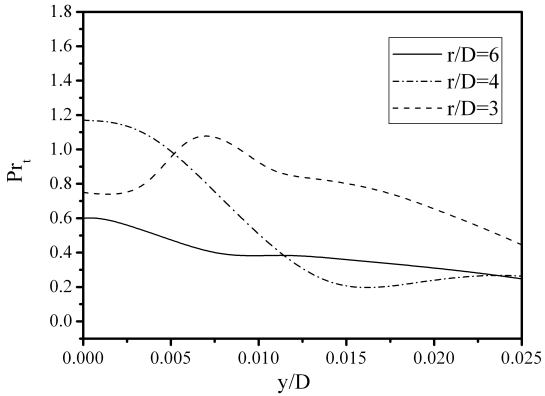

Figure 5.2: Turbulent Prandtl number distribution at r/D=3, 4 and 6 (obtained from LES).

purpose the Nusselt number data (at H/D=6) from experiments of Baughn and Shimizu [12], Baughn et al. [13] and Lytle and Webb [131] have been used. It is found that the Kay's correlation ([111])for turbulent Prandtl number gives good results near the stagnation zone. Unfortunately, the differences in experimental data are too high. Therefore, no final conclusion can be made on the quality of the correlation.

5.2 Calibration of Coefficients

The scalar-flux models coefficients are determined through the method based on the non-linear least-squares algorithms. The coefficients are analysed for the following models:

- Daly and Harlow [32]
- Abe and Suga [2]
- Younis et al. [199]

5.2.1 Daly and Harlow Model

The model is based on the gradient diffusion hypothesis (GDH). The coefficient for this model is obtained from the LES data analysis and plotted in figure 5.3(a) and 5.3(b). It is

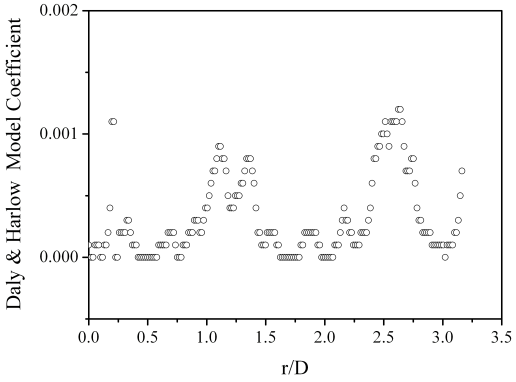

(a)

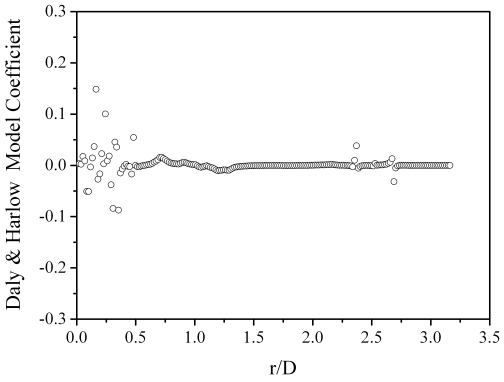

(b)

Figure 5.3: Daly and Harlow model [32] coefficient distribution close to target wall from (a) $\overline{u_y'T'}$ at y/D=1$\times$ 10^{-03} and from (b) $\overline{u_r'T'}$ at y/D=0.02. The symbol shows the model coefficients obtained from LES data.

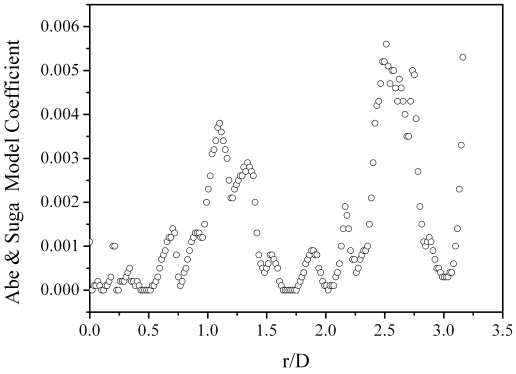

(a)

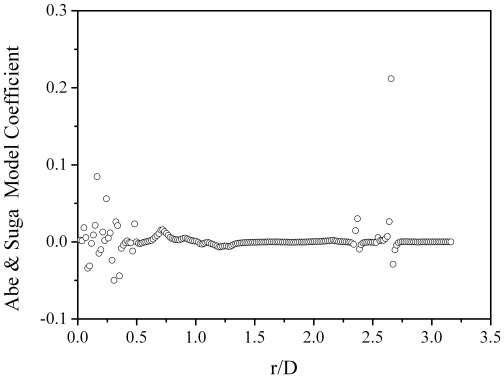

(b)

Figure 5.4: Abe and Suga model [2] coefficient distribution from (a) $\overline{u_y' T'}$ at y/D=1$\times$ 10^{-03} and from (b) $\overline{u_r' T'}$ at y/D=0.02. The symbol shows the model coefficients obtained from LES data.

found that the original value of the coefficient for this model, 0.3 is too high for heat transfer prediction in impinging jet case. The maximum value of the $C_{\theta 1}$ estimated from LES data analysis is found to be 0.15.

5.2.2 Abe and Suga Model

The model coefficient for this model is investigated. The original value of the coefficient recommended for this model is 0.6. The value estimated from LES data analysis is found to be much lower. The coefficient for this model is obtained from the LES data analysis and plotted in figure 5.5(a) and 5.5(b). The maximum value of the $C_{\theta 2}$ estimated from LES data analysis is around 0.2.

Both Daly and Harlow model and Abe and Suga model have incorporated the gradient diffusion hypothesis. It is interesting to note that the trend of the coefficient distribution is similar to the Daly and Harlow model. The similitude in trend is an indication of the dominating role of GDH in Abe and Suga model. Recently, Abe has stressed the importance of GDH for the scalar-flux modeling in impinging jet case [3].

5.2.3 Younis et al. Model

The coefficients of the Younis et al. model are investigated using radial $\overline{u_r' T'}$ and vertical $\overline{u_y' T'}$ distributions. In both cases, C_3 and C_4 are found to be more sensitive than the other coefficients. The coefficients of C_1, C_2, C_3 and C_4 are plotted in figure 5.5. In the Younis et al. model, the coefficient C_3 is found to be varying a lot and C_4 is showing large swing near the stagnation point. A polynomial is fitted to the coefficient data. The mean, standard deviation and coefficient of determination are reported in table 5.1. The closer the coefficient of determination is to 1, the more completely the fitted model explains the data. However, from the practical point of view this approach reduces the robustness and generality of the model. Because of large oscillations in the optimized coefficient values, it is important to analyze the role of each term in detail.

Table 5.1: **Coefficients of Younis et al. model [199]**

Coeff.	Original value	Mean	Standard Deviation	Coefficient of Determination
C_1	- 0.0455	- 0.0481	0.008	0.468
C_2	+ 0.373	+ 0.3723	0.0017	0.3424
C_3	- 0.00373	+ 0.0028	0.0084	0.432
C_4	- 0.0235	- 0.0195	0.0087	0.784

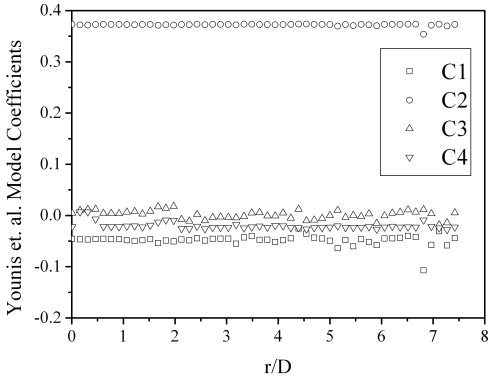

(a)

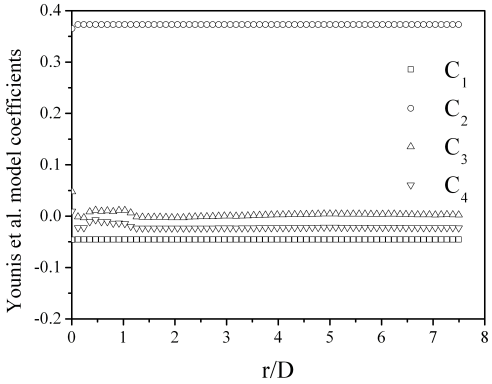

(b)

Figure 5.5: Younis et al. model [199] coefficients distribution at (a) y/D=1$\times$ 10^{-03}, computed from $\overline{u_y^{'}T^{'}}$ (b) at y/D=0.02, computed from $\overline{u_r^{'}T^{'}}$.

According to Younis et al. the functional relation of these terms in the scalar-flux is:

$$\begin{aligned} Scalar\ flux\ = \quad & \text{Gradients of scalar } [\, C_3\ (Mean\ velocity\ gradients) \\ & +C_4\ (Production\ rate)] \end{aligned} \tag{5.9}$$

The C_3 term and C_4 term represent the effect of the production terms and scalar gradients, is originated from the Dakos and Gibson (1987) model for fluctuating pressure and scalar-gradients [33]. Kataoka et al. [108] have found that large scale eddies of surface pressure turbulence play an important role in an impinging jet. Therefore the inclusion of these terms in the scalar-flux model is justified. However the analysis through LES data shows that the model coefficients for these terms needs to be adjusted. Figure 5.6 (c) and (d) shows that the Younis et al. model under-predicts the effect of this term at the stagnation point. To compensate this effect the value of C_3 in general and C_4 is found through optimization.

Further, it has been found that near the jet's stagnation point, the first term of Younis et al. model is playing a dominant role and important for the stagnation modeling. The term actually represent the Gradient Diffusion Hypothesis.

5.3 Similarity of Mechanical and Thermal Time Scales

An important issue in scalar-flux modeling is the similarity of mechanical and thermal time scales. The flow (r_m) and thermal scales (r_t), used in scalar-flux models, are defined as:

$$r_m = \frac{k}{\varepsilon} \tag{5.10}$$

$$r_t = \frac{\overline{T'T'}}{\varepsilon_t} \tag{5.11}$$

ε_t can be estimated from the asymptotic relation, used for specification of boundary conditions in scalar-flux models as:

$$\varepsilon_t = \alpha(\partial\sqrt{(\overline{T'T'})}/\partial y)^2 \tag{5.12}$$

It is clear from figure 5.7 that the assumption of same heat and mechanical scales is very far from reality.

The coefficients of scalar flux models determined from LES are tested in the commercial CFD code, CFX-sp11. For the flow field the model implemented by Dietz [39] at ITLR has been used. It incorporates the specific dissipation rate and the dissipation rate tensor

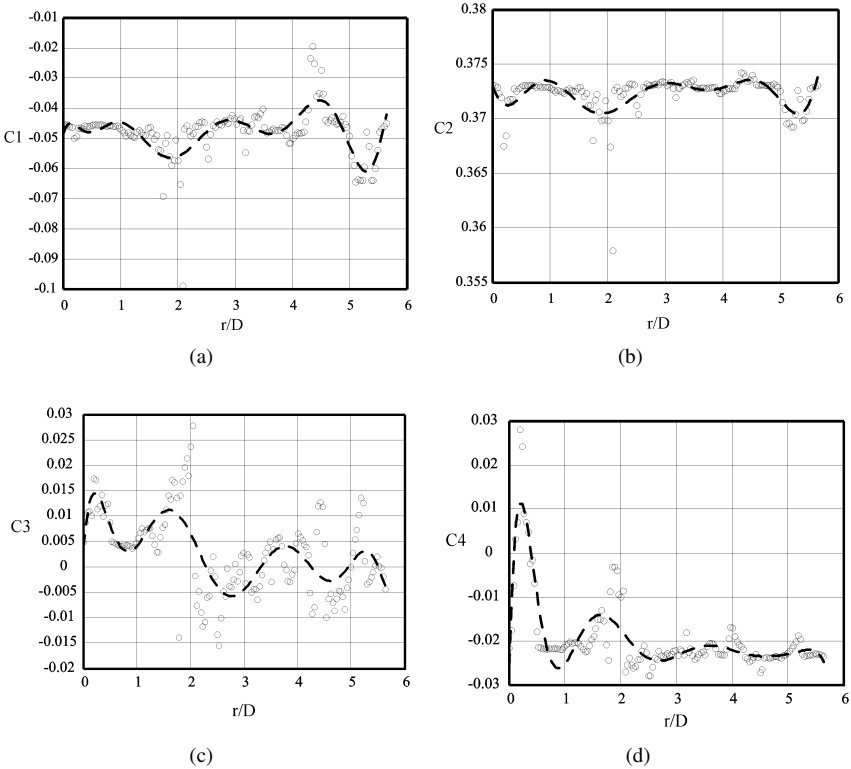

Figure 5.6: Curve fitting of the coefficient distribution at y/D=1$\times$ 10^{-03}, (Younis et al. model) computed from $\overline{u_y' T'}$.

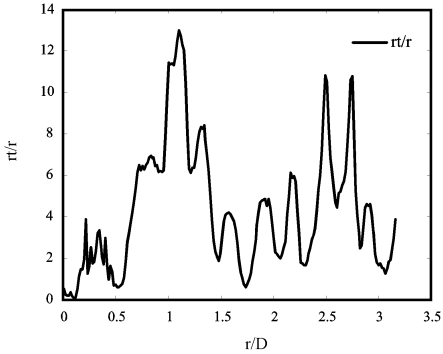

Figure 5.7: Ratio of the mechanical (r_m) and heat (r_t) time scales at at y/D=1$\times$ 10^{-03}.

is modified based on the Rotta and Kolmogorov approaches [193; 164]. The wall reflection term is used for modeling of pressure-correlation based on modifications proposed by Speziale, Sarkar and Gatski (SSG) [176]. The low Reynolds number damping function proposed by Gullman and Strand is also included [71].

No significant changes in the model behaviors were found when C_3 and C_4 are changed. The radial distribution of the Nusselt number predicted by different scalar flux models is plotted in figure 5.8. The Low Reynolds number SSG model, is found to be incapable of predicting the secondary peak. All three models were found to be behaving in a similar fashion in case of an impinging jet. Here, it is important to note that the indirect influence of flow turbulence model can significantly alter the scalar-flux predictions, as the mechanical time scale is a quantity independent of the scalar-flux model. The scalar flux models are based on the turbulent fluctuations and correct predictions of them in the near wall region is crucial for the correct flow field prediction. The flow field predicted by Low Re SSG model is shown in figure 5.9(a) and 5.9(b).

The Anisotropy invariant map in the wall jet at r/D = 2 from the Low Reynolds SSG model and LES data is plotted in figure 5.10. The low Reynolds number SSG model predict that in an impinging jet the near wall flow is isotropic and follows the axisymmetric expansion state like channel or duct flows. This is contrary to what has been found through experiments and LES and discussed in previous chapter, that the flow near wall is following the axisymmetric contraction state. Further the magnitude of second and third invariants is underpredicted. This shows that the complete Reynold stress tensor is underpredicted by

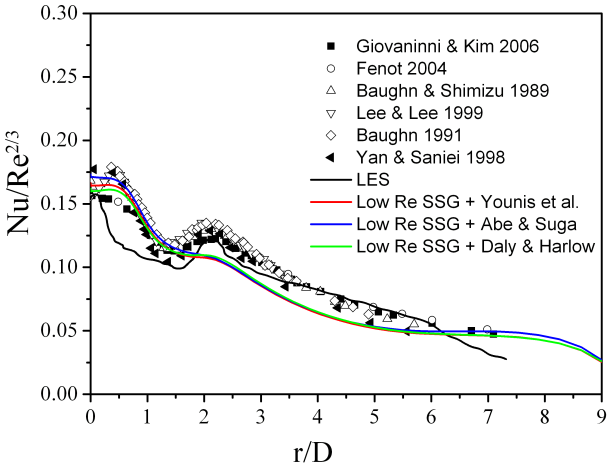

Figure 5.8: Radial distribution of the Nusselt number from the Low Reynolds SSG model and scalar flux models.

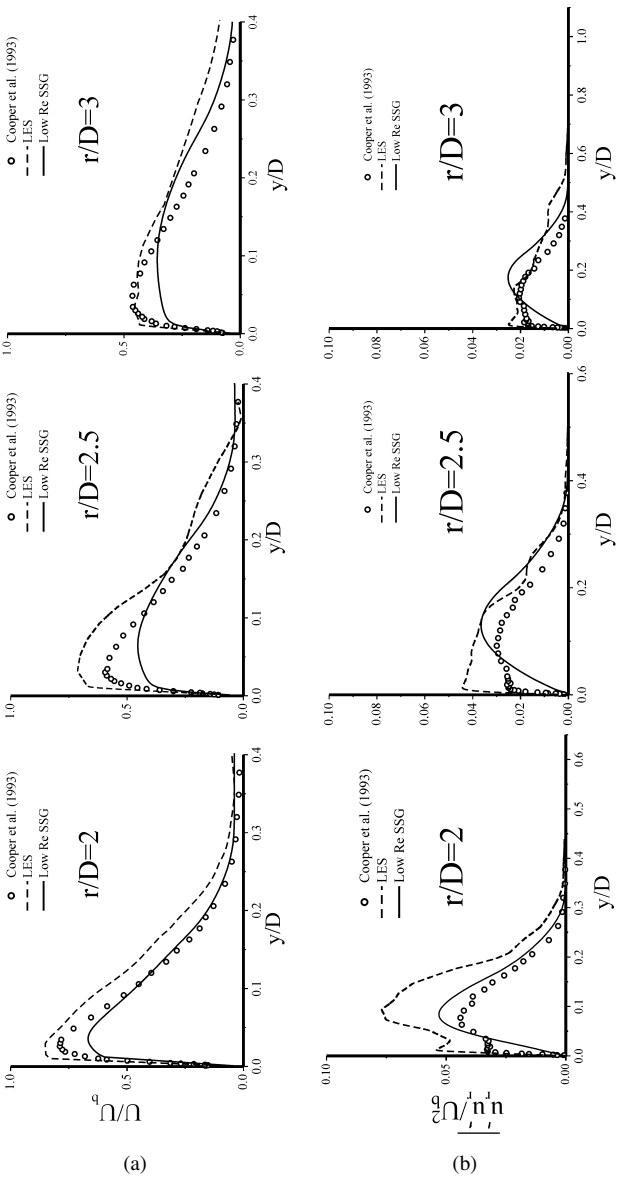

Figure 5.9: Prediction of (a) mean velocity and (b) $\overline{u_r' u_r'}$ from Low Reynolds SSG model in wall jet.

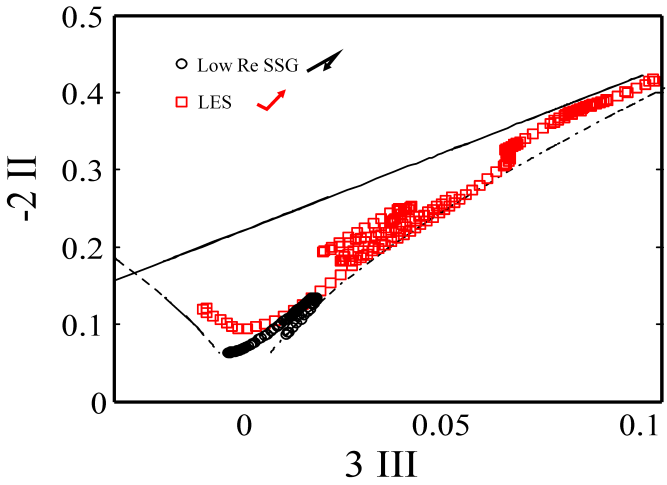

Figure 5.10: Anisotropy invariant map in wall jet at r/D = 2 from Low Reynolds SSG model and LES (till y/D = 0.04). The lines with arrow in the legend show the trend of distribution.

the model. In this situation, one can expect that the mechanical time scale is also underpredicted.

As the turbulent fluctuations are underpredicted near the wall, the level of the $\overline{u_i' T'}$ will also be underpredicted. However, the scalar-flux underprediction is corrected by the high values of the coefficients used in the scalar-flux models. Therefore, although the turbulent quantities are underpredicted, heat transfer predicted by the scalar-flux models is in satisfactory agreement with the experimental data.

The above analysis based on the Large Eddy Simulation data gives better insight in an impinging jet phenomenon which would help in devising better turbulence models for RANS based computations.

6. CONCLUSIONS

The dynamics of flow and heat transfer in an impinging jet is very complex involving jet stagnation, ring vortex impact, acceleration of flow and then deceleration. The addition of swirl and pulsations make the flow further complex. Large Eddy Simulations provide the detailed information of the flow and heat transfer fields which is difficult to get in details by present experimental techniques.

First, a Large Eddy Simulation of an impinging jet at Reynolds number of 23000 and (jet's) outlet-to-target distance of two diameter has been conducted. The flow statistics are compared with known experimental results. The most amplified frequency is found to be present in the jet's shear layer. This frequency is found to be very close to free jet, indicating the undisturbed nature of the jet. Several harmonic frequencies were found in the wall jet zone, indicating the complex flow structural dynamics.

It is found that the mean velocity in the wall jet can be cast into scaling log-laws. In order to highlight the reason of the failure of the RANS based turbulence models, the anisotropy invariant map is utilized. The flow is found to be anisotropic near the wall which means that the RANS models based on isotropy assumption may not work well for this case. The production of turbulent kinetic energy is found to be negative in distinct regions very close to wall. This also indicates one of probable reason of the failure of the RANS models. The turbulent Prandtl number is evaluated and found to be varying from 0.6 to 1.2 in non-linear fashion. The reason of peaks in the radial distribution of the Nusselt number were investigated. The previously proposed interpretations for the peaks are outlined and discussed, which helps in understanding the underlying phenomenon causing the appearance of the peaks in the distribution of the Nusselt number.

In case of the velocity field excitation it is found that the excitation of the jet velocity field causes only large scale excitation. It is interesting to note that the slope of the spectrum is independent of the excitation. The excitation at higher frequencies gives rise to non-linear interactions between the scales and the jet receptivity to the excitational frequencies higher than the preferred mode becomes lower. This causes the reduction in the most amplified frequency. The inlet velocity field is excited at four different frequencies. It is found that the excitation at harmonic frequencies causes the formation of small vortical structures

which are less able to improve mixing and enhance heat transfer. This makes the harmonic excitation less effective. In case of natural (unforced) jet the turbulent kinetic energy is concentrated at the location of the secondary peak. In case of forced jet, the turbulent kinetic energy is high in the wall jet zone but the distribution is uniform, causing the secondary peak to be flattened or removed.

The passive excitation of the jet through an excitational device like cylindrical insert in the pipe is investigated. The device can generate the flow fluctuations which can bring forth the enhancement in the heat transfer. It is found that the heat transfer is greatly improved by the use of such device.

The investigation of the effects of excitation of jet's inlet temperature field on heat transfer is a pioneering work. The jet's inlet temperature field is excited at three different frequencies. In case of the temperature field excitation, it is found that the surface-averaged Nusselt number is high when the jet is excited at its preferred mode. The excitation at the subharmonic frequency gives the highest heat transfer at the stagnation point. However on excitations at higher harmonic frequencies the scalar variance shows sudden increase, which is an indicator of thermal fluctuations experienced by the target wall. Therefore, in some cases depending on the material of the target wall it is should be monitored for safe operation.

The turbulent swirling jet impingement has been simulated with different Reynolds numbers and swirl numbers. It is found that in case of the swirling jet, the increase in swirl causes the jet breakdown before the impingement. It is noticed that the high temperature fluid is trapped in recirculation zone which causes the deterioration of the heat transfer in the *geometric stagnation* region. The addition of the swirl to the jet creates multiple impingement zones which causes the shift in the location of maximum heat transfer at the target wall. In case of high swirl number, the peak in radial distribution of the Nusselt number is better correlated with the occurrence of maximum turbulent kinetic energy close to wall. However at small swirl number the peak in the radial distribution of the Nusselt number is better correlated with the approaching velocity. The swirl gives no perceptible increase in overall heat transfer for H/D=2 case.

The simulation data is used for the investigation of the relationship between turbulence quantities and scalar-fluxes. The coefficients of the RANS based scalar-flux models are originally validated for the heat transfer estimation for simple flow cases. The investigation of different scalar-flux models through LES data of an impinging jet shows that coefficients in the models need adjustment. However, it is important to note that in RANS equations not the turbulent heat flux but its spatial derivative is important. Also, the prediction from scalar-flux models depends a lot on the accompanying turbulence model. Therefore in some cases the turbulence model may overcome the deficiencies of scalar-flux model and it could deliver the acceptable results. Through the investigation it is found that commonly held

assumption of similar flow and thermal scales utilized in scalar-flux modeling is a drastic simplification. It is found that the surface pressure driven scalar-flux transport mechanism is dominant and must be accounted in the heat transfer modeling for prediction of the complex phenomenon of impinging jet. The results found through LES data give better insight in the flow phenomenon, which will help in devising new turbulence models for RANS based computations.

REFERENCES

[1] K. Abe, T. Kondoh, Y. Nagano, 1994, *A new turbulence model for predicting fluid flow and heat transfer in separating and reattaching flows- I. Flow field calculations*, Int. J. Heat and Mass Transfer, Vol. 37, No. 1, 139 - 151.

[2] K. Abe, K. Suga, 2001, *Towards the development of a Reynolds-averaged algebric turbulent scalar-flux model*, Int. J. Heat and Fluid Flow, Vol. 22, 19 - 29.

[3] K. Abe, *Performance of Reynolds-averaged turbulence and scalar flux models in complex turbulence with flow impingement*, Progress in Computational Fluid Dynamics, **6**, No 1/2/3, 79 - 88 (2006).

[4] Antonopoulous-Domis, 1981, *Large eddy simulation of passive scalar in isotropic turbulence*, J. Fluid Mech., Vol. 104, 55 - 79.

[5] J. K. Abrantes, L. F. A. Azevedo, 2006, *Fluid flow and heat transfer characteristics of a swirl jet impinging on a flat plate*, Annals of the Assembly for International Heat Transfer Conference 13.

[6] T. Akiyama, K. Yamamoto, K. D. Squires, K. Hishida, 2005, *Simulation and measurement of flow and heat transfer in two planar impinging jets*, Int. J. of Heat and Fluid Flow, Vol. 26, 244 - 255.

[7] M. Angioletti, E. Nino, G. Ruocco, 2005, *CFD turbulent modelling of jet impingment and its validation by particle image velocimetry and mass transfer measurements*, Int. J. Thermal Sciences, Vol. 44, 349 - 356.

[8] `http://www.ansys.com/products/icemcfd.asp`.

[9] S. Ashforth-Frost, K. Jambunathan, C. F. Whitney, S. J. Ball, 1997, *Heat transfer from a flat plate to a turbulent axisymmetric impinging jet*, Proc. Instn. Mech. Engrs., Vol. 211 Part C, 167 - 172.

[10] S. Ashforth-Frost, K. Jambunathan, C. F. Whitney, 1997, *Velocity and turbulence characteristics of a semi-confined orthogonally impinging slot jet*, Exp. Thermal and Fluid Science, Vol. 14, 60 - 67.

[11] L. F. A. Azevedo, B. W. Webb, M. Queiroz, 1994, *Pulsed Air Jet Impingement Heat Transfer*, Exp. Thermal and Fluid Science, Vol. 8, 206 - 213.

[12] J. W. Baughn, S. Shimizu, 1989, *Heat transfer measurement from a surface with uniform heat flux and an impinging jet*, Int. J. of Heat Transfer, Vol. 111, 1096 - 1098.

[13] J. W. Baughn, A. E. Hechanova, X. Yan, 1991, *An experimental study of entrainment effects on the heat transfer from a flat surface to a heated circular impinging jet*, J. Heat Transfer, Vol. 113, 1023 - 1025.

[14] M. Behnia, S. Parneix, P.A. Durbin, 1998 *Prediction of heat transfer in an axisymmetric turbulent jet impinging on a flat plate*, Int. J. Heat and Mass Transfer, Vol. 41, No.12, 1845 - 1855.

[15] L. C. Berselli, T. Iliescu, W. J. Layton, 2006, *Mathematics of Large Eddy Simulation of Turbulent Flows*, Springer.

[16] M. Bohnert, J. H. Ferziger, 1993, *The dynamic subgrid scale model in large-eddy simulation of the stratified Ekman layer*, Engg. Turb. Moel. & Exp. 2, 315 - 324, Elsevier.

[17] M. P. Boyce, 2002, *Gas Turbine Engineering Handbook*, Gulf Professional Publishing.

[18] J. M. Buchlin, 2000, *Aero-thermal Performance of internal cooling systems in turbomachines*, Von Karman institute for Fluid Dynamics Lecture series 2000- 03.

[19] J. Bardina, J. H. Ferziger, W. C. Reynolds, 1983, *Improved turbulence modelsbased on large eddy simulation o homogeneous compressible turbulent flows*, Rep no. TF-19, Thermoscience division, Standford University, USA.

[20] M. Breuer, 2002, *Direkte Numerische Simulation und Large-Eddy Simulation turbulenter Strömungen auf Höchleistungrechnern*, Habilitation thesis, Shaker Verlag.

[21] C. Camci, F. Herr, 2002, *Forced Convection heat transfer enhancement using a self-oscillating impinging planar jet*, J. Heat Transfer, Vol. 24, 770 - 782.

[22] I. Celik, M. Klein, M. Freitag, J. Janika, *Assessment measures for URANS/DES/LES:an overview with applications*, J. Turbulence, Vol. 7, 1, 1 - 27.

[23] Y. M. Chung, K. H. Luo, N.D. Sandham, 2002, *Numerical study of momentum and heat transfer in unsteady impinging jets*, Int. J. Heat and Fluid Flow, 23, 592 - 600.

[24] Y. M. Chung, K. H. Luo, 2002, *Unsteady heat transfer analysis of an impinging jet*, J. Heat Transfer, Vol. 124, 1039 - 1048.

[25] M. Ciofalo, *Large-Eddy simulation: A critical survey of models and applications*, Advances in Heat Transfer, Volume 25

[26] M. Coussirat, J. Van Beeck, M. Mestres, E. Egusguiza, J. M. Buchlin, X. Escaler, 2005, *Computational fluid dynamics, modeling of impinging gas-jet systems:I. Assessment of eddy viscosity models*, J. Fluid Engg., Vol. 127, 691- 703.

[27] T. Colonius, 1997, *Numerically nonreflecting boundary and interface conditions for compressible flow and aeroacoustic computations*, J. AIAA, Vol. 35, No. 7, 1126-1133.

[28] D. Cooper, D. C. Jackson, B. E. Launder, G. X. Liao, 1993, *Impinging jet studies for turbulence model assessment- I. Flow field experiments*, Int. J. Heat and Mass Transfer, Vol 36, No. 10, 2675 - 2684.

[29] T. J. Craft, L. J. Graham, B. E. Launder, 1993, *Impinging jet studies for turbulence model assessment- II. An examination of the performance of four turbulence models*, Int. J. Heat and Mass transfer, Vol. 36, No. 10, 268 5 - 2697.

[30] T. Cziesla, E. Tandogan, N. K. Mitra, 1997, *Large Eddy Simulation of heat transfer from impinging slot jets*, Num. Heat Transfer, Part A, Vol. 32, 1 - 17.

[31] T. Cziesla, G. Biswas, H. Chattopadhyay, N. K. Mitra, 2001, *Large Eddy Simulation of flow and heat transfer in an impinging slot jet*, Int. J. Heat and Fluid Flow, Vol. 22, 500 - 508.

[32] B. J. Daly, F. H. Harlow, 1970, *Transport equations in turbulence*, Phy. Fluids, Vol. 13, No. 11, 2634- 2649.

[33] T. Dakos, M.M. Gibson, 1987, *On modelling the pressure terms of the scalar flux equations*, 7 - 18, Turbulent Shear flows 5, Springer.

[34] J. W. Deardorff, 1970, *A numerical study of three dimensional turbulent channel flow at large Reynolds number*, J. Fluid Mech., Vol. 41, 453.

[35] J. W. Deardorff, 1973, *Three dimensional numerical modeling of planetary boundary layer, Workshop on Micrometerology*, Chapter 7, 271-311, Am. Meteorol. Soc. Boston.

[36] J. W. Deardorff, 1970, *A three dimensional numerical investigation of the idealized planetary boundary layer*, Geophy. Fluid Dynamics, 1, 377 -410, 1970.

[37] J. W. Deardorff, 1980, *Stratcumulus-capped mixed layers derived from a three-dimensional model*, Boundary layer Meterorol., 32, 205 - 236.

[38] N. Didden, Chih-Ming. Ho, 1985, *Unsteady separation in a boundary layer produced by an impinging jet*, J. Fluid Mech., Vol. 160, 235 - 256.

[39] C. Dietz, 2008, *Computational heat transfer of internal flows with vortex-inducing elements*, Universität Stuttgart, Germany.

[40] S. J. Downs, E. H. James, 1987, *Jet impingement heat transfer- a literature survey*, ASME paper 87-H-35.

[41] P.A. Durbin, B. A. Pettersson Reif, 2001, *Statistical theory and modelling for turbulent flows*, John Wiley & Sons Ltd.

[42] J. G. M. Eggels, F. Unger, M. H. Weiss, J. Westerweel, R. J. Adrian, R. Friedrich, F. T. M. Nieuwstadt, 1994, *Fully developed turbulent pipe flow: A comparison between direct numerical simulation and experiment*, J. Fluid Mech. 268, 175 - 209.

[43] `http://cfd.mace.manchester.ac.uk/ercoftac/`.

[44] M. Fairweather, G. K. Hargrave, 2002, *Experimental investigation of an axisymmetric impinging turbulent jet. 1. Velocity field*, Exp. Fluids, Vol. 33, 464 - 471.

[45] Parallel Multigrid Solver for Flows in Complex Geometries, Flow Predictor Description, Lehrstuhl fuer Stroemungsmechanik, Universität Earlangen-Nuernberg.

[46] FASTEST User Manual, 2005, Department of Numerical Methods in Mechanical Engineering, Technische Universität Darmstadt.

[47] M. Fenot, 2004, *Etude du refroidissement par impact de jets. application aux aubes de turbines*, Université de Poitiers, PhD Dissertation, France.

[48] M. D. Fox, M. Kurosaka, L. Hedges, K. Hirano, 1993, *The influence of vortical structures on the thermal fields of jets*, J. Fluid Mech., Vol. 255, 447- 472.

[49] J. Ferziger, 1996, *Large Eddy simulation, Simulation and modeling of Turbulent flows*, Edited by Thomas B. Gatski, M. Yousuff Hussaini, John L. Lumley, Oxford University Press.

[50] J. H. Ferziger, M. Peric, 1999, *Computational methods for fluid dynamics*, Springer Verlag.

[51] Fachgebiet für Numerische Berechnungsverfahren im Maschinenbau (FNB), Technische Universität, Darmstadt, Germany.

[52] C. F. Gago, F. Garnier, F. Utheza, 2003, *Direct testing of subgrid scale models in large-eddy simulation of a non-isothermal turbulent jet*, Int. J. Num. Methods in Fluids, Vol. 42, 999 - 1026.

[53] C. Gau, W. Y. Sheu, C. H. Shen, 1997, *Impingment cooling flow and heat transfer under acoustic excitations*, J. Heat Transfer, Vol. 119, 810 - 817.

[54] C. Gau, C. C. Lee, 1992, *Impingement cooling flow structure and heat transfer along rib- roughened walls*, Int. J. Heat and Mass transfer, Vol. 35, 3009 - 3020.

[55] S. Gao, D.C. Leslie, P.R. Voke, 1991, *Large eddy simulation of thermal impinging jets*, Rep ME-FD/91.02 Dep. Mech. Eng., University of Surrey, Guildford, UK.

[56] S. Gao, P. R. Voke, 1995, *Large Eddy Simulation of turbulent heat transport in enclosed impinging jets*, Int. J. Heat and Fluid Flow, Vol. 16, 349 - 356.

[57] X. Gao, B. Sunden, 2003, *Experimental investigation of the heat transfer characteristics of confined impinging slot jets*, Experimental Heat Transfer, Vol. 16, 1 - 18.

[58] R. Gardon, J. Cobonpue, 1962, *Heat transfer between a flat plate and jets of air impinging on it*, Int. Developments in Heat Transfer, 454 - 460, ASME New York.

[59] R. Gardon, J. C. Akfirat, 1965, *The role of turbulence in determining the heat transfer characteristics of impinging jet*, Int. J. Heat and Mass Transfer, Vol. 8, 1261 - 1272.

[60] R. Gardon, J. C. Akfirat, 1966, *Heat transfer characteristics of impinging two dimensional air jets*, Int. J. Heat and Mass Transfer, Vol. 88, 101 - 108.

[61] L. F. G. Geers, M. J. Tummers, K. Hanjalic, 2004, *Experimental investigation of impinging jet arrays*, Exp. Fluids, Vol. 36, 946 - 958.

[62] L. F. G. Geers, K. Hanjalic, M. J. Tummers, 2006, *Wall imprint of turbulent structures and heat transfer in multiple impinging jet arrays*, J. Fluid Mech., Vol. 546, 255 - 284.

[63] D. R. S. Guerra, J. Su, A. P. S. Feire, 2005, *The near wall behaviour of an impinging jet*, Int. J. Heat and Mass Transfer, 48, 2829 - 2840.

[64] M. Germano, U. Piomelli, P. Moin, W. H. Cabot, 1991, *A dynamic subgrid-scale eddy viscosity model*, Phy. Fluid A 3 (7), 1760 - 1765.

[65] A. Giovannini, N. S. Kim, 2006, *Impinging jet: Experimental analysis of fluid field and heat transfer for assesment of turbulent models*, Annals of the Assembly for International Heat Transfer Conference 13, 2006, TRB-15.

[66] R. J. Goldstein, A. I. Behbahani, K. K. Heppelmann, 1986, *Stream-wise distribution of the recovery factor and the local heat transfer coefficient to an impinging circular air jet*, Int. J. Heat and Mass Transfer, Vol. 29, No. 8, 1227 - 1235.

[67] R. J. Goldstein, K. A. Sobolik, W. S. Seol, 1990, *Effect of entrainment on the heat transfer to a heated circular air jet impinging on a flat surface*, J. of Heat Transfer, Vol. 112, 608 - 611.

[68] R. J. Goldstein, J. F. Timmers, 1982, *Visualisation of heat transfer from arrays of impinging jets*, Int. J. Heat and Mass Transfer, 25, 1857 - 1868.

[69] R. J. Goldstein, W. S. Seol, 1991, *Heat transfer to a row of impinging circular air jets including the effect of entrainment*, Int. J. Heat and Mass Transfer, Vol. 34, No.8, 2133 - 2147.

[70] G. Grötzbach and M. Wörner, 1999, *Direct numerical and large eddy simulations in nuclear applications*, Int. J. Heat and Fluid Flow, 20, 222 -240.

[71] J. Gullman-Strand, 2004, *Turbulence and scalar flux modelling applied to separated flows*, Royal Institute of Technology.

[72] A. K. Gupta, D. G. Lilley, N. Syred, 1984, Swirl Flows, Gordon & Breach Science Publishers.

[73] E. Gutmark, C. Ho, 1983, *Preferred modes and the spreading rates of jets*, Phy. Fluids, Vol. 26, No. 10, 2932-2938.

[74] H. Hattori, Y. Nagano, 2004, *Direct numerical simulation of turbulent heat transfer in plane impinging jet*, Int. J. of Heat and Fluid Flow, Vol. 25, 749 - 758.

[75] J. W. Hall, D. Ewing, 2005, *The development of the large-scale structures in round impinging jets exiting long pipes at two Reynolds numbers*, Exp. Fluids, Vol. 38, 50 - 58.

[76] B. Han, R. J. Goldstein, 2001, *Jet-impingement heat transfer in Gas Turbine systems*, Annals of New York Academy of Sciences, Vol. 934, 147 - 161.

[77] J. C. Han, S. Dutta, S. Ekkad, 2000, *Gas turbine heat transfer and cooling technology*, Taylor & Francis.

[78] M. Hadžiabdić, 2005, *LES, RANS and Combined Simulation of Impinging Flows and Heat Transfer*, PhD. Thesis, TU Delft

[79] T. Hällqvist, 2006, *Large-eddy simulation of impinging jets with heat tansfer*, PhD Thesis, Royal Institute of Technology, Department of Mechanics, Sweden.

[80] G. K. Hargrave, T. C. Williams, K. Anandarajah, N. A. Halliwell, 2006, *The 3D Velocity Field of an Impacting Turbulent Jet*, Second International Conference on Optical and Laser Diagnostics (ICOLAD 2005), J. of Physics: Conference Series, 45, 162 - 172.

[81] K. Hanjalić, 2005, *Turbulence and transport phenomenon modelling and simulation*, Darmstadt.

[82] K. Heyerichs, A. Pollard, 1996, *Heat transfer in separated and impinging turbulent flows*, Int. J. Heat and Mass Transfer, Vol. 12, 2385 - 2400.

[83] `http://www.hlrs.de/`.

[84] C. M. Ho, N. S. Nossier, 1981, *Dynamics of impinging jet. Part 1, the feedback Phenomenon*, J. Fluid Mech., Vol. 105, 119 - 142.

[85] C. M. Ho, L.S. Huang, 1982, *Subharmonics and vortex merging in mixing layers*, J Fluid Mech., Vol. 119, 443 - 473.

[86] H. M. Hofmann, 2005, *Wärmeübergang beim pulsierenden prallstrahl*, Dissertation, Universität Karlsruhe.

[87] C. J. Hoogendoorn, 1977, *The effect of turbulence on heat transfer at a stagnation point*, Int. J. Heat and Mass Transfer, Vol. 20, 1333 - 1338.

[88] L. Huang, M. El-Genk, 1994, *Heat transfer of an impinging jet on a flat surface*, Int. J. Heat and Mass Transfer, Vol. 137, No. 13, 1915 - 1923.

[89] L. Huang, M. S. El-Genk, 1998, *Heat transfer and flow visualization experiments of swirling, multi-channel, and conventional jets*, J. Heat and Mass Transfer, Vol. 41, No 3, 583 - 600.

[90] J. C. R. Hunt, A. A. Wray, P. Moin, 1988, *Eddies, stream and convergence zones in turbulent flows*, Center for Turbulence Research, CTR-S88, Stanford University.

[91] J. C. Hunter, M. H. Tsai, J.F. Lockett, P.R. Voke, M.W. Collin, D.C- Leisle, 1988, *A comparison of large eddy simulation predictions of a thermal layer with holographic interferrometry*, Proc. Int. conf. Numer. Methods Therm. Prob. 5th Montreal.

[92] S. D. Hwang, C. H. Lee, H. H. Cho, 2001, *Heat transfer and flow structures in axisymmetric impinging jet controlled by vortex pairing*, Int.J. Heat and Fluid flow 22, 293 - 300.

[93] S. D. Hwang, H. H. Cho, 2003, *Effects of acoustic excitation positions on heat transfer and flow in axisymmetric impinging jet: main jet excitation and shear layer excitation*, Int. J. of Heat and Fluid Flow, Vol. 24, 199 - 209.

[94] A. K. M. F. Hussain, K. B. M. Q. Zaman, 1980, *Vortex pairing in circular jet under controlled excitation. part2. Coherent structure dynamics*, J. Fluid Mech., Vol. 101, 493 - 544.

[95] A. K. M. F. Hussain, 1983, *Coherent structures - reality and myth*, Phy. Fluids, Vol. 26, No. 10 , 2816 - 2850.

[96] H. Herwig, H. Mocikat, Gürtler, S. Göppert, 2004, *Heat transfer due to unsteadily impinging jets*, Int. J. of Thermal Sciences 43, 733 - 741.

[97] A. A. Khalatov, A. A. Avramenko, I. V. Shevchuk, 2000, *Heat transfer and fluid flow in the fields of centrifugal forces, Swirl flows*, Vol.-III, (russian edition), National Academy of sciences of Ukraine, Institute of Engineering Thermophysics, Kiev.

[98] FASTEST, 2001, Invent Computing, GmbH.

[99] 2005, *The jet engine*, Rolls-Royce plc.

[100] K. Jambunathan, E. Lai, M. A. Moss, B. L. Button, 1992, *A review of heat transfer data for single circular jet impingement*, Int. J. Heat and Fluid Flow, Vol. 13, No. 2, 106 - 115.

[101] R. Jia, M. Rokni, B. Sunden, 2002, *Numerical assessment of different turbulence models for slot jet impinging on flat and concave surfaces*, Proceedings of ASME Turbo Expo, June, Amsterdam, Netherlands.

[102] M. Jischa, H. B. Rieke, 1979, *About the prediction of turbulent Prandtl and Schmidt numbers from modified transport equations*, Int. J. of Heat and Mass Transfer, 22, 1547.

[103] W. P. Jones, P. Musonge, 1988, *Closure of Reynolds stress and scalar flux equations*, Phy. Fluids, Vol. 31, No. 12, 3589 - 3604.

[104] P. Jiang, Y. C. Guo, C. K. Chan, W. Y. Lin, 2007, *Frequency characteristics of coherent structures and their excitations in small aspect-ratio rectangular jets using large eddy simulation*, Computers & Fluids 36, 611 - 621.

[105] X. Jiang, H. Zhao, K.H. Luo, 2007, *Direct computation of perturbed impinging hot jets*, Computers & Fluids 36, 259 - 272.

[106] T. Kobayashi, M. Kano, T. Ishihara, 1985, *Prediction of turbulent flow in two dimensional channel with turbulence promoters*, Bull. JSME 28 (246), 2948 - 2953.

[107] N. Kasagi, Y. Tomita, A. Kuroda, 1992, *Direct numerical simulation of passive scalar field in a turbulent channel flow*, J. Heat Transfer, Vol. 114, 598 -606.

[108] K. Kataoka, Y. Kamiyama, S. Hashimoto, T. Komi, 1982, *Mass transfer between a plane surface and an impinging turbulent jet: the influence of surface-pressure fluctuations*, J. of Fluid Mech., 119, 91 - 105.

[109] K. Kataoka, M. Suguro, H. Degawa, K. Maruo, I. Mihata, 1987, *The effect of surface renewal due to large scale eddies on jet impingement heat transfer*, Int. J. Heat and mass Transfer, No. 3, Vol. 30, 559 - 567.

[110] J. Kim, P. Moin, R. Moser, 1987, *Turbulence statistics in fully developed channel flow at low Reynolds number*, J. Fluid Mech. 177, 133 - 166.

[111] W. M. Kays, M. E. Crawford, B. Weigand, 2004, *Convective Heat and Mass Transfer*, McGraw-Hill.

[112] J. Kim, P. Moin, 1989, *Transport of passive scalars in a turbulent channel flows*, Turbulent shear flows, Vol.6, 85 - 96, Springer, Berlin.

[113] D. Kwack, W. C. Reynolds, J. H. Ferziger, 1975, *Three dimensional time dependent computation of turbulent flows*, Rep No. TF-5, Dept. Mech. Eng. Stanford Unoversity, USA.

[114] P. Krogstad, L. E. Torbergsen, 2000, *Invariant Analysis of Turbulent Pipe Flow*, Flow, Turbulence and Combustion 64, 161 - 181.

[115] M. Klein, A. Sadiki, J. Janicka, 2003, *A digital filter based generation of inflow data for spatially direct numerical or large eddy simulations*, J. of Comp. Physics 18, 652 - 665.

[116] B. Lakshminarayana, 1996, *Fluid dynamics and heat transfer of turbomachinery*, John Wiely & Sons.

[117] C. C. Landreth, R. J. Adrian, 1990, *Impingement of a low Reynolds number Turbulent circular jet onto a flat plate at normal incidence*, Exp. Fluids 9, 74 - 84.

[118] B. E. Launder, 1988, *On the computation of convective heat transfer in complex flows*, Vol. 110, J. of Heat Transfer, 1112 - 1128

[119] B. E. Launder, 1978, *Turbulence*, Topics in Applied Physics, edited by P. Bradshaw, Vol 12, Springer.

[120] D. Lee, R. Greif, S. J. Lee, J. H. Lee, 1995, *Heat transfer from a flat plate to a fully developed axisymmetric Impinging jet*, J. Heat Transfer, Vol. 117, 772 -776.

[121] J. Lee, S. Lee, 1999, *Stagnation region heat transfer of a turbulent axisymmetric jet impingement*, Exp. Heat Transfer, 12, 137 - 156.

[122] J. Lee, S. J. Lee, 2002, *The effect of nozzle configuration on stagnation region heat tranfsfer enhancement of axisymmetric jet impingement*, Int. J. Heat and Mass Transfer, 43, 3497- 3509.

[123] D. H. Lee, S. Y. Won, T. T. Kim, Y. S. Chung, 2002, *Turbulent heat transfer from a flat surface to a swirling round impinging jet*, Int. J. of Heat and Mass Transfer, 45, 223 - 227.

[124] D. H. Lee, J. Song, M. C. Jo, 2004, *The effects of nozzle diameter on impinging jet heat transfer and fluid flow*, J. of Heat Transer, Vol. 126, 554 - 557.

[125] M. Lesieur, O. Metais, P. Comte, 2005, *Large-Eddy Simulatios of Turbulence*, Cambridge University Press.

[126] A. Leonard, 1996, *Direct numerical Simulation of Turbulent flows, Simulation and modeling of Turbulent flows*, Edited by Thomas b. Gatski, M. Yousuff Hussaini, John L. Lumley, Oxford University Press.

[127] D. K. Lilly, 1966, *On the application of eddy viscosity concept in the inertial sub-range of turbulence*, Rep NCAR-123, Natinal Center for Atmospheric Research, Boulder, USA.

[128] T. Liu, J. P. Sullivan, 1996, *Heat transfer and flow structures in an excited circular impinging jet*, Int. J. Heat and Mass Transfer, 17: 3695 - 3706.

[129] H. Lugt, 1983, *Vortex flows in Nature and Technology*, Wiley & Sons.

[130] T. Lund, X. Wu, D. Squires, 1998, *Generation of turbulent inflow data for spatially-developing boundary layer simulations*, J. Comp. Phy. 140, 233- 258.

[131] D. Lytle, B. W. Webb, 1994, *Air jet impingment heat transfer at low nozzle-plate spacing*, Int. J. Heat and Mass Transfer, Vol. 137, No. 12, 1687 - 1697

[132] D. K. Lilly, 1992, *A proposed modification of the Germano subgrid-scale closure method*, Phy. Fluid, A, Vol. 4, N. 3, 633 - 635.

[133] H. Martin, 1998, *Waermeuebergang bei Prallstroemung*, VDI-Waermeatlas, VDI.

[134] D. M. Markovich, *Particle Image Velocimetry and its application in Impinging Jet Flows*, Presentation of Heat Transfer International Presentation of Heat Transfer International Research Institute (HTI), Brussels, ULB, 8 June, 2005, Institute of Thermophysics SB RAS.

[135] E. C. Mladin, D.A. Zumbrunnen, 1997, *Local convective heat transfer to submerged pulsating jets*, Int. J. Hea Transfer, Vol. 40 (14) 3305- 3321.

[136] E. C. Mladin, D. A. Zumbrunnen, 1995, *Dependence of heat transfer to a pulsating stagnation flow on pulse characteristics*, J. of Thermophysics and Heat Transfer, Vol. 9, No.1, 181 - 191.

[137] E. C. Mladin, D. A. Zumbrunnen, 2002, *Alterations to coherent flow structures and heat transfer due to pulsations in an impinging air-jet*, Int. J. Therm. Sci, Vol. 39, 236 - 248.

[138] P. Moin, J. Kim, 1981, *Numerical investigation of turbulent channel flow*, NASA Tech. Memo. NASA TM-81309.

[139] P. Moin, K. Squires, W. Cabot, S. Lee, 1991, *A dynamic subgrid scale model for compressible turbulence and scalar transport*, Phys. Fluids,

[140] O. Mětais, M. Lesieur, 1992, *Spectral large eddy simulation isotropic and stabiliy stratified turbulence*, J. Fluid Mech., Vol. 239, 157 - 194.

[141] H. Martin, 1977, *Heat and mass transfer between impinging jets and solid surfaces*, Advances in Heat Transfer, Vol. 13, 1 - 60.

[142] B. Merci, I. Vierendeels, C. DeLange, E. Dick, 2003, *Numerical simulation of heat transfer of turbulent impinging jet with two equation turbulence models*, Int. J. Num. Methods of Heat and Fluid flow, Vol. 13, 110 - 132.

[143] P. J. Mason, N. S. Callon, 1986, *On the magnitude of subgrid scale eddy coefficient in large edy simulations of turbulent channel flow*, J. Fluid Mech., 162, 439 - 462.

[144] P. Moin, K. Mahesh, 1998, *Direct Numerical Simulation: A tool in turbulence research*, Ann. Rev. Fluid Mech., Vol. 30, 539 - 78.

[145] C. H. Moeng, J. C. Wyngaard, 1988, *Spectral analysis of large eddy simulations of convective boundary layers*, J. Atmos. Sci Vol. 45 (23), 3573 - 3587.

[146] R. G. Nevins, H. D. Ball, 1961, *Heat transfer between a flat plate and a pulsating impinging jet*, National Heat Transfer Conference Boulder, CO, ASME.

[147] K. Nishino, M. Samada, K. Kasuya, K. Torii, 1996, *Turbulence statistics in the stagnation region of an axisymmetric impinging jet flow*, Int. J. Heat and Fluid Flow, Vol. 17, 193 - 201.

[148] A. Nozaki, Y. Igarashi, K. Hishida, 2003, *Heat transfer mechanism of a swirling impinging jet in a stagnation region*, Heat Transfer Asian research, Vol. 32, (8), 663 - 673.

[149] M. Olsson, L. Fuchs, 1998, *Large Eddy Simulations of a forced semi-confined circular impinging jet*, Phys. Fluid, Vol. 10, No. 2, 476 - 486.

[150] I. B. Özdemir, J. H. Whitelaw, 1992, *Impingement of an axis-symmetric jet on unheated and heated flat plates*, J. Fluid Mech., Vol. 240, 503 - 532.

[151] J. Panda, D. K. McLaughlin, 1994, *Experiments on the instabilities of a swirling jet*, Phy. of fluid, Vol. 6, No 1, 263 - 276.

[152] T. S. Park, H. J. Sung, 2001, *Development of near wall turbulence model and application to jet impingment heat transfer*, Int. J. Heat Fluid Flow, Vol. 22, 10 - 18.

[153] T. H. Park, H. G. Choi, J. Y. Yoo, S. J. Kim, 2003, *Streamline upwind numerical simulation of two dimensional confined impinging slot jets*, Int. J. Heat and Mass Transfer, Vol. 46, 251 - 262.

[154] S. Parneix, M. Behnia, P. A. Durbin, 1999, *Prediction of turbulent heat transfer in an axis-symmetric jet impinging on a heated pedestal*, J. Heat Transfer, 1999, 121: 43 - 49.

[155] U. Piomelli, J.H. Ferziger, P. Moin, J. Kim, 1989, *New approximate boundary conditions for large eddy simulation of wall bounded flows*, Phy. Fluids A 1 (6), 1061 - 1068.

[156] U. Piomelli, H. Cabot, P. Moin, S. Lee, 1991, *Subgrid-scale backscatter in turbulent and transitional flows*, Phy. Fluids A, 3(7), 1766 - 1771.

[157] S. Polat, A. S. Mujumdar, W. J. M. Douglas, 1985, *Heat transfer distribution under a turbulent impinging jet- a numerical study*, Drying Technology, Vol. 3, No. 1, 15 - 38.

[158] S. Polat, B. Huang, A. S. Mujumdar, W. J. M. Douglas, 1989, *Numerical flow and heat transfer under impinging jets, a review*, Annual Review of Numerical Fluid Mechanics and Heat Transfer, Vol. 2, 157 - 197.

[159] C. O. Popiel, O. Trass, 1991, *Visualisation of a free and impinging round jet*, Exp. Thermal and Fluid Sciences, 4: 253 - 264.

[160] C. O. Popiel, T. H. Van der Meer, C. J. Hoogendoorn, 1980, *Convective heat transfer on a plate in an impinging round hot gas jet of low Reynolds number*, Int. J. Heat and Mass Transfer, Vol. 23, 1055 - 1068.

[161] Cz. O. Popiel, L. Boguslawski, 1986, *Mass or heat transfer in impinging single, round jets emitted by a bell-shaped nozzle and Sharpe-ended orifice*, Proceedings of 8th Int. Heat transfer Conference, San Francisco, CA, USA, Vol. 3.

[162] M. Poreh, Y. G. Tsuei, J. E. Cermak, 1967, *Investigation of a turbulent radial wall jet*, J. of App. Mech., 34, 457- 463.

[163] M. M. Rogers, N. Mansour, W. C. Reynolds, 1989, *An algebric model for turbulent flux of a passive scalar*, J. Fluid Mech., Vol. 203, 77 - 101.

[164] J. C. Rotta, 1972, *Turbulente Strömungen*, B. G. Teubner Stuttgart.

[165] J. Revstedt, J. Gullbrand, F. Guillard, L. Fuchs, C. Trägardh, 1998, *Large Eddy Simulations of mixing in an impinging jet*, Proceeding of fourth European Computational fluid dynamics conference , Athens , Greece. John Wiley and Sons.

[166] M. H. Rizk, S. Menon, 1988, *Large eddy simulations of axis-symmetric excitation effects on a row of impinging jets*, Phy. of Fluids 31, 7, 1892 - 1903.

[167] D. J. Sailor, D. J. Rohli, Q. Fu, 1999, *Effect of variable duty cycle flow pulsations on heat transfer enhancement for an impinging air jet*, Int. J. Heat and Fluid Flow, Vol. 20, 574 - 580.

[168] J. Sakakibara, K. Hishida, 1997, Masanobu Maeda, *Vortex structure and heat transfer in the stagnation region of an impinging plane jet (simultaneous measurements of velocity and temperature field by digital particle image velocimetery and laser induced fluorescence)*, Int. J. Heat and Mass Transfer, Vol. 40, No. 13, 3163 - 3176.

[169] S. Satake, T. Kunugi, *Direct numerical simulation of an impinging jet into parallel disks*, Int. J. num. Methods Heat Fluid Flow, Vol.8, no. 7, 768 - 780, 1998.

[170] M. Schaefer, 2006, *Computational Engineering Introduction to Numerical Methods*, Springer.

[171] U. Schumann, 1975, *Subgrid scale model for finite difference simulations of turbulent flows in a plane channels and annuli*, J. Comp. Phys 18, 376- 404.

[172] M. Senda, K. Inaoka, D. Toyoda, S. Sato, 2005, *Heat Transfer and Fluid Flow Characteristics in a Swirling Impinging Jet*, Heat Transfer Asian Research, 34 (5), 324 - 335.

[173] H.S. Sheriff, D.A. Zumbrunnen, 1994,*Effect of flow pulsation on cooling effectiveness of an impinging jet*, J. of Heat Transfer, Vol. 116, 886- 895.

[174] R. M. So, T. P. Sommer, 1996, *An explicit heat flux model for the temperature field*, Int. J. Heat and Mass Transfer, Vol. 39, 455- 465.

[175] J. S. Smagorinsky, 1963, *General circulation experiments with the primitive equations: 1. The basic experiment*, Mon. Weather. Rev. 91 (3), 99 - 164.

[176] C. G. Speziale and S. Sarkar and T. B. Gatski, 1991, *Modelling the pressure-strain correlation of turbulence: an invariant dynamical systems approach*, J. Fluid Mech., 227, 245-272.

[177] S. A. Stanley, S. Sarkar, J. P. Mellado, 2002, *A study of the flow-field evolution and mixing in a planar turbulent jet using direct numerical simulation*, J. Fluid Mech., Vol. 450, 377 - 407.

[178] H. L. Stone, 1988, *Iterative solution of implicit approximations of multidimensional partial differential equations*, SIAM J. Numer. Anal. 5 (3), 530 - 558.

[179] S. A. Striegl, T. E. Diller, 1984, *An analysis of the effect of entrainment temperature on jet impingement heat transfer*, J. Heat Transfer, Vol. 106, 804 - 810.

[180] K. Suga, K. Abe, 1999, *Nonlinear eddy viscosity modelling forturbulence and heat transfer near wall and shear-free boundaries*, In Int. J. of Heat and Fluid Flow, Vol. 21, pages 37-48. Elsevier.

[181] F. O. Thomas, 1991, *Structure of mixing layers and jets*, App. Mech. Review, 44, 119 - 153.

[182] A. Tsinober, 2004, *An Informal Introduction to Turbulence*, Fluid Mechanics and its Applications, Kluwer Academic Publishers.

[183] M. Tsubokura, A. T. Kobayashi, N. Taniguchi, W. P. Jones, 2003, *A numerical study on the eddy structures of impinging jets excited at the inlet*, Int. J. of Heat and Fluid Flow, Vol. 24, 500 - 511.

[184] J. Vejražka, 2002, *Experimental study of pulsating round impinging jet*, PhD. Thesis, Institute of Chemical Process Fundamentals, Prage.

[185] R. Viskanta, 1993, *Heat transfer to impinging Isothermal Gas and Flame jets*, Exp. Thermal and Fluid Sciences , 6: 111 - 134.

[186] P. R. Voke, S. Gao, D. Leslie, 1995, *Large Eddy simulations of Plane impinging jets*, Int. J. for Numerical Methods in Engineering, Vol. 38, 489 - 507.

[187] P. R. Voke, S. Gao, 1998, *Numerical study of heat transfer from an impinging jet*, Int. J. Heat and Mass Transfer, Vol. 41, 671 - 680.

[188] J. Ward, M. Mahmood, 1982, *Heat transfer from a turbulent swirling impinging jet*, Proceedinds of 7th Int. Heat Transfer Conference, 3: 401 - 408.

[189] B. Wegner, Y. Huai, A. Sadiki, 2004, *Comparative study of turbulent mixing in jet in cross-flow configurations using LES*, Int. J. of Heat and Fluid Flow, Vol. 25, 767 - 775.

[190] D. C. Wilcox, 1993, *Turbulence modeling for CFD*, 2nd Ed., DCW Industries.

[191] M. Wen, K. Jang, 2003,*An impingement cooling on a flat surface by using circular jet with longitudinal swirling strips*, Int. J. of Heat and Mass Transfer 46, 4657 - 4667.

[192] P. M. Wikström, S. Wallin, A. V. Johansson, 2000,*Derivation and investigation of a new explicit algebric model of the passive scalar flux*, Phy. of Fluids, Vol. 12, No. 3, 688- 702.

[193] D. C. Wilcox, 1988, *Reassessment of the scale-determining equation for advanced turbulence models*, AIAA Journal, 26, 1299 - 1310.

[194] I. Wygnanski, Y. Katz, E. Horev, 1992, *On the aplicability of various scaling laws to the turbulent wall jet*, J. Fluid Mech., 234, 669- 690.

[195] X. Yan, N. Saniei, 1998, *Heat Transfer Measurements From a Flat Plate to a Swirling Impinging Jets*, Proceedings of 11th Int. Heat Transfer Conference, Kyonju, Korea.

[196] X. T. Yan, R. S. Kalvakota, 2006, *Numerical Analysis of local heat transfer from a flat plate to a swirling air impinging jet*, Proceedings of IMECE2006, ASME Int. Mechanical Engineering Congress and Exposition, Chicago, Illinois, USA.

[197] S. Yokobori, N. Kasagi, M. Hirata, 1983, *Transport phenomenon at the stagnation region of a two-dimensional impinging jet*, Transactions of JSME B, 49;441, 1029 - 1039.

[198] A. J. Yule, 1981, *Investigation of eddy coherence in jet flows, The role of coherent structures in modelling turbulence and mixing*, lecture notes in physics-136, Springer Verlag.

[199] B. A. Younis, C. G. Speziale, T. T. Clark, 2005, *A rationale model for turbulent scalar fluxes*, Proceedings of the Royal Society A, Vol. 461, 575 - 594.

[200] B. A. Younis, B. Weigand, S. Spring, 2007, *An explicit algebraic model for turbulent heat transfer in wall-bounded flow with streamline curvature, J. of Heat Transfer*, 127, 425 -433 (2007).

[201] D.A. Zumbrunnen, M. Aziz, 1993, *Convective heat transfer enhancement due to intermittency in an impinging jet*, J. Heat Transfer, Vol. 115, 91 - 98.

[202] D. A. Zumbrunnen, 1992, *Transient convective heat transfer in planar stagnation flows with time-varying surface heat flux and temperature*, J. of Heat Transfer, Vol. 114, 85 - 93.

[203] D. A. Zumbrunnen, M. Balasubramanian, 1995, *Convective heat transfer enhancement due to gas injection into an impinging liquid jet*, J. Heat Transfer, Vol. 117, 1011- 1017.

[204] N. Zuckerman, N. Lior, 2005, *Impingment heat transfer: correlations and numerical modeling*, J. Heat Transfer, Vol. 127, 544 - 552.

APPENDIX

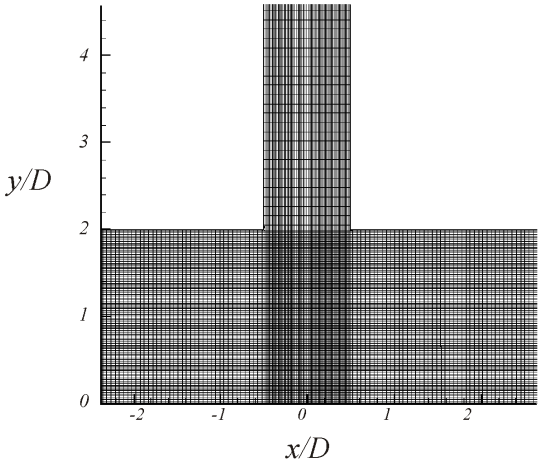

(a)

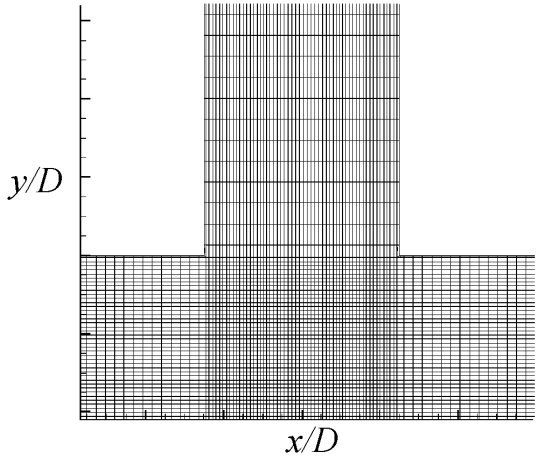

(b)

Figure .1: Grid used for the investigation of unexcited/excited jet impingement, (a) Grid view in cross-section, only the zone (-2 < x/D < 2) is shown. (b) Close up at the jet's outlet.

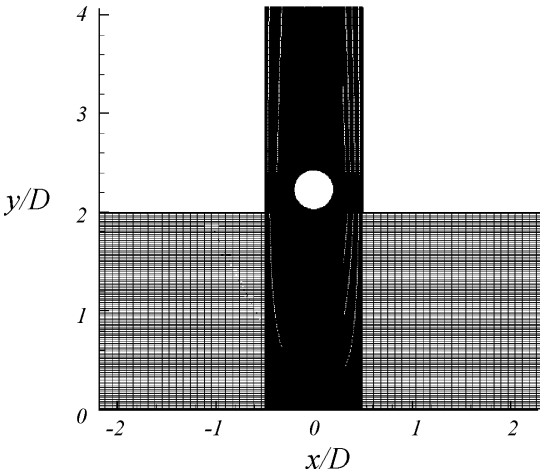

(a)

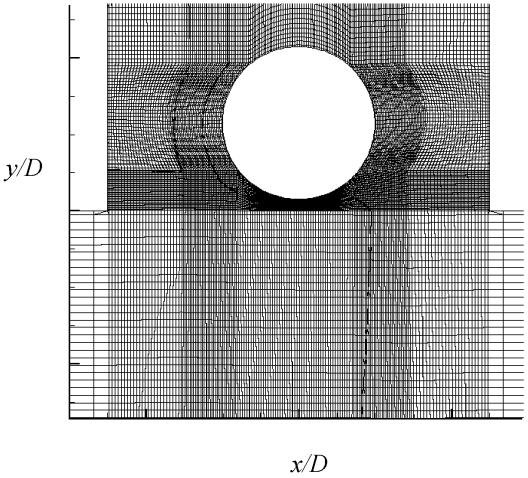

(b)

Figure .2: Grid used for the investigation of passively excited jet impingement, (a) view in cross-section, only the zone (-2 < x/D < 2) is shown. (b) close-up at the jet's outlet.

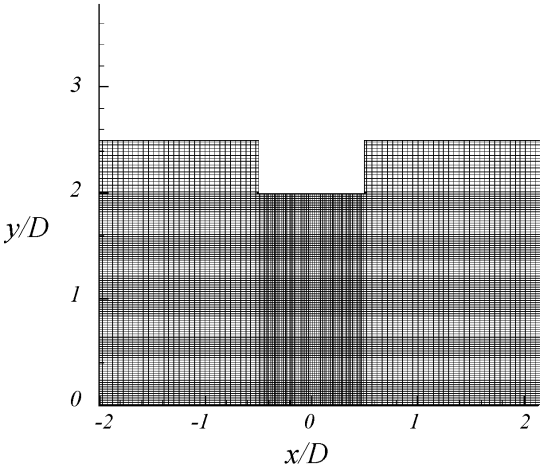

(a)

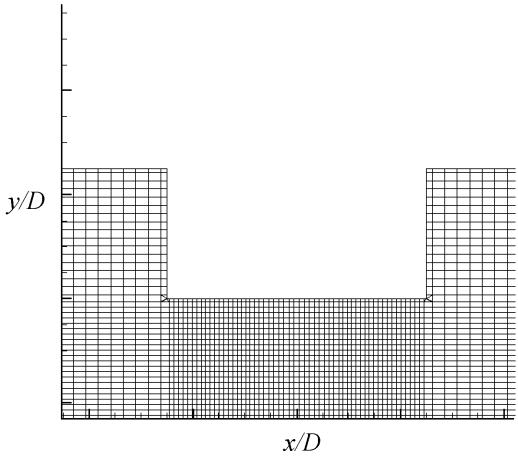

(b)

Figure .3: Grid used for the investigation of swirling jet impingement, (a) view in cross-section, only the zone (-2 < x/D < 2) is shown. (b) close-up at the jet's outlet.

Curriculum Vitae

Name	Naseem Uddin
Marital status	married, one son
Email Address	Naseem.Uddin@itlr.uni-stuttgart.de heatransfer@yahoo.com
Qualifications	
2002	Master of Mechanical Engineering, NED University of Engineering & Technology, Karachi, Pakistan.
1996	Bachelor of Mechanical Engineering, NED University of Engineering & Technology, Karachi, Pakistan.
Experience	
2004 - 2008	Research Associate at Institute of Aerospace Thermodynamics, Universität Stuttgart, Germany.
2002 - 2008	Assistant Professor at Mechanical Engineering Department, NED University of Engineering & Technology, Karachi, Pakistan.
1999 - 2002	Lecturer at Mechanical Engineering Department, NED University of Engineering & Technology, Karachi, Pakistan